Journal of Environmental Management 373 (2025) 123705

Contents lists available at ScienceDirect

Journal of Environmental Management

journal homepage: www.elsevier.com/locate/jenvman

Research article

The development of multifunctional biochar with $NiFe_2O_4$ for the adsorption of Cd (II) from water systems: The kinetics, thermodynamics, and regeneration

Makhosazana Masuku, Jemal Fito Nure *, Harrison I. Atagana, Ntuthuko Hlongwa, Thabo T.I. Nkambule **

Institute for Nanotechnology and Water Sustainability (iNanoWS), College of Science, Engineering and Technology, Florida Science Campus, University of South Africa, Johannesburg, South Africa

ARTICLE INFO

Keywords:
Adsorbent
Heavy metal
Kinetics
Reusability
Thermodynamics
Water treatment

ABSTRACT

High concentrations of Cd (II) in wastewater have been reported several times which attracted top research attention to mitigate the pollution impacts of the contaminant. Therefore, this study aimed to develop a Zn-doped $NiFe_2O_4$ pinecone biochar composite (ZNiF@PB) for the adsorption of Cd (II) from wastewater. FTIR confirmed immobilization of PB on the surface of ZNiF by the presence of C = O at 1638 cm^{-1}, COOH at 1385 cm^{-1}, C-O at 1009 cm^{-1} and Fe-O at 756 cm^{-1}. Similarly, XRD determined the crystallite structure of the adsorbents where the ZNiF crystallite size of 43 nm was obtained while the particle size of ZNiF@PB was found to be 38 nm. These XRD results agreed with those values obtained from TEM images showing ZNiF and ZNiF@PB had a spherical shape with similar particle sizes. On the other hand, the surface areas of ZNiF, PB, and ZNiF@PB were found to be 78.4 m^2/g, 125 m^2/g, and 104 m^2/g, respectively. These high surface areas have a huge potential to enhance Cd removal. With these adsorbents, the maximum Cd (II) adsorption of 96% was recorded at the optimum experimental condition of adsorbent dosage 0.5g/50 mL, solution pH 6, initial Cd (II) concentration 100 mg/L, and contact time 120 min. Practical adsorption kinetics data were well described by the pseudo-second order model whereas the adsorption isotherm was a perfect fit to the Langmuir isothermal model implying the adsorption process to be a monolayer with mainly a chemically bonded mechanism. In conclusion, this adsorbent is efficient for the adsorption of Cd (II) from wastewater and has also a huge potential to be applied for industrial-scale water purification.

1. Introduction

The rapid increase in chemical industries has resulted in the continuous production of wastewater that contains high concentrations of toxic contaminates. In particular, heavy metals are nondegradable and can pass through the food chain to cause biological magnification. This, in turn, may adversely impact public and environmental health. Chromium, arsenic, lead, and cadmium are some of the heavy metals present in water bodies (Mitra et al., 2022; Qi et al., 2024). Cadmium particularly has more severe effects compared to other heavy metals (Mitra et al., 2022). It emanates from industries such as the mining sector, metal electroplating, smelting, tanning, paints, zinc sulfide ores, batteries, industrial processes, and pigments (Limmun et al., 2024). Similarly, pesticides and fertilizers increase cadmium-containing effluent, especially in countries that practice most agricultural activities (Limmun et al., 2024). The acceptable concentration of cadmium in drinking water by the World Health Organization (WHO) is 0.005 mg/L (Limmun et al., 2024). However, the cadmium concentration in contaminated wastewater is between a few mg/L to >150 mg/L (Nakajima et al., 2022; Zeng et al., 2019). Therefore, to investigate, the best test for the treatment of high-concentration cadmium-containing wastewater effluent was 150 mg/L. There are many health effects associated with breathing air containing cadmium, ingesting food, and drinking water with high concentrations of cadmium (Limmun et al., 2024). Short-term exposure to cadmium can cause skin, eye irritation, and nausea, while long-term contact causes cancer and damages the

* Corresponding author.
** Corresponding author.
E-mail addresses: fitojemal120@gmail.com (J.F. Nure), nkambtt@unisa.ac.za (T.T.I. Nkambule).

https://doi.org/10.1016/j.jenvman.2024.123705
Received 21 July 2024; Received in revised form 19 November 2024; Accepted 10 December 2024
Available online 17 December 2024

spinal cord, brain, nervous system, and internal organs of both humans and aquatic organisms (Alorabi et al., 2022; Chatzimichailidou et al., 2023; Shakya et al., 2022).). Therefore, it is necessary and of great urgency to develop highly efficient and economical treatment methods for cadmium-containing wastewater.

Various water treatment techniques including membrane filtration, chemical precipitation, coagulation-flocculation, ion exchange, and adsorption are explored and applied to eliminate toxic cadmium from effluents (Fito et al., 2023a; Limmun et al., 2024; Mitra et al., 2022; Qi et al., 2024). However, most of them have major drawbacks including chemical precipitation that requires large settling tanks, ion exchange is limited by regeneration problems, coagulation-flocculation is disadvantaged by low removal efficiency and chemical requirements, and membrane filtration shortcomings involving the production of large amounts of sludge, as well as the cost challenges associated with sludge disposal (Azari et al., 2015). Furthermore, high initial and operational costs, high energy consumption, and poor selectivity have also been reported (Kakavandi et al., 2018; Omidinasab et al., 2018). Among these methods, adsorption is considered one of the most effective and efficient routes based on the advantages of simplicity of design, cost-effectiveness, flexibility, high pollutant removal, less toxicity, and good reusability (Kakavandi et al., 2018; Limmun et al., 2024; Massoudinejad et al., 2015). To fully explore the advantages of adsorption, an appropriate adsorbent must be used (Kakavandi et al., 2014; Masuku et al., 2022; Qi et al., 2024). An ideal adsorbent must possess a high surface area, rapid adsorption, high performance, cost-economical, less toxicity, ease of separation, and must be reusable (Babaei et al., 2015; Moges et al., 2022). For the removal of cadmium from wastewater, commonly investigated adsorbents include carbon nanotubes, zeolites, activated carbon, clay minerals, organic polymers such as resins, chitosan, char ash, biochar, and metal oxides, etc. (Abolfazli Behrooz et al., 2023; Amen et al., 2020; Bai et al., 2023; Deng et al., 2019; Hu et al., 2022; Qi et al., 2024; Singh et al., 2018). Most of these adsorbents have shown good adsorption efficiencies in eliminating metals from aquatic resources, for example, activated carbon (Fito et al., 2023c). However, activated carbon has certain limitations and these limitations have therefore driven researchers to the new generation of adsorbents called metal oxides. Metal oxides are classified as orthoferrite ($MFeO_3$), garnet ($M_3Fe_5O_{12}$), hexagonal crystal structure ($BaFe_{12}O_{19}$ and $SrFe_{12}O_{19}$), and spinel ferrite MFe_2O_4 (Herein, M = Mg, Cu, Ni, Co Zn, etc.). The first and most promising choice of newly developed metal oxides for the removal of cadmium from wastewater is spinel ferrite. In the spinel structure, the divalent M^{2+} is occupied at the tetrahedral site, while the trivalent Fe^{3+} is placed at the octahedral site (Dehghani Dastjerdi et al., 2023). Thus far, this nanoadsorbent shows the most promise because of its excellent properties, such as superparamagnetic properties, tunable morphology, sizeable surface area, plenty of sorption sites, high pollutant removal efficiency, simple separation with magnet substance, and reusability (Olfatmehr et al., 2022; Punia et al., 2022; Tatarchuk et al., 2021). Regrettably, the use of spinel ferrite is limited by its nonselective nature and poor stability in aqueous solution, as its particles become easily aggregated, which equally affects their adsorption efficiency (Limmun et al., 2024). However, the drawbacks of this adsorbent can be curbed by the necessary surface modification. Therefore, effective surface modification for spinel ferrite nanoparticles using a green material such as biochar that has many effective oxygen groups, including ketones, carboxyl, hydroxyl, amines, etc. has drawn increasing interest in water research. Generally, biochar is a carbonaceous material obtained from the pyrolysis of biomass from sustainable sources (Ahmed et al., 2023; Wang et al., 2021). It has multiple advantages, such as porous structure, environmental friendliness, and easy preparation (Ahmed et al., 2023; Wang et al., 2021). Many biochar adsorbents that have been used include rice husk, banana peels, coconut shells, pine bark, orange peels, avocado peels, ground nut shells, and pinecones with high affinity for heavy metals (Ahmed et al., 2023; Bai et al., 2023; Lee and Park, 2020; Shakya et al., 2022; Van Vinh et al., 2015). However, the physicochemical properties of biochar and their adsorption properties towards a specific heavy metal differ based on their biomass sources. The interaction between spinel ferrite and biochar has been reported in previous work for the removal of heavy metals from wastewater. For example, $MnFe_2O_4$/Zn-Fe/rice straw was used to remove cadmium ions and recorded 75.1% [17], $MnFe_2O_4$-Zn-Fe/soybean straw used to remove 76.9% of cadmium from wastewater [17], $MnFe_2O_4$–Zn ferrite/pine sawdust was used to remove 80.1% lead from wastewater [35], Fe–Mn/Rice straw used to remove 92.2% cadmium [89]. Similarly, 91.6% of cadmium was removed by $MnFe_2O_4$/pine sawdust (Niu et al., 2020), 76.5% of nickel was adsorbed with $MgFeAlO_4$/rice bran biochar (Guo et al., 2020), 95% of Cr(VI) and As(V) was eliminated using Fe_2O_3/raspberries stalks (Dobrzyńska et al., 2022), 99.8% of As(III) was adsorbed by $CuFe_2O_4$@pine sawdust (Wang et al., 2023), and 92.4% silver was trapped using $CoFe_2O_4$/Citrus sinensis/Citrus reticulata peels (Mahmoud et al., 2022). Based on these results, it is fair to assume that the use of spinel ferrite-coated biochar as an adsorbent is a promising material for future wastewater treatment applications if it is explored fully. However, the effectiveness of the adsorbent could be attributed to the properties of the individual materials. For example, spinel ferrite has good magnetism, and biochar has a porous structure and effective oxygen groups. Therefore, the interaction between these two adsorbents can form a nanocomposite with unique features, superior stability, excellent magnetic properties, good surface structure, low ecotoxicity, and easy separability (reusability). This feature can improve the sorption performance. Furthermore, this adsorbent has low toxicity levels and is environmentally friendly (Fito and Nkambule, 2023; Masuku et al., 2024). Although many spinels of ferrite@biochar have been reported in the literature, limited information from the search database on the application of zinc-doped nickel ferrite (ZNiF) nanoparticles modified by biochar has been available, which points out a research gap in this technology. The lack of previous studies on ZNiF@biochar adsorbents is the driving force for this study to close the research gap. Conclusive evidence from the literature suggests that ZNiF@biochar is suitable for cadmium adsorption research work and has been scarcely reported. Herein, pristine Zn-doped ZNiF and pine cone biochar (PB) were reported in the study. In addition, a simple two-step method was employed to prepare ZNiF@PB) for the adsorption of cadmium from wastewater. Fundamentally, the Zn-doped $NiFe_2O_4$ ferrite material is chemically stable which is an excellent choice for the fabrication of an environmentally functional adsorbent that will not result in secondary contamination (Ahangari et al., 2019). Furthermore, Zn-doped $NiFe_2O_4$ has a high saturation magnetization; therefore, the magnetic separation of the adsorbent after application can be carried out efficiently through the support of an external magnetic field. This will allow the magnetic adsorbent to be recycled several times, solving the drawbacks of biochar materials, which include the fact that it is not easily separated after applications and requires complex procedures. Furthermore, the addition of Zn-doped $NiFe_2O_4$ to pinecone biochar can change the carbonization material of pinecone and give more surface area and more active sites for sorption purposes (Ahangari et al., 2019; Kang et al., 2022). Therefore, this study aimed to develop a Zn-doped $NiFe_2O_4$- pinecone biochar composite (ZNiF@PB) for the adsorption of Cd (II) from wastewater. The study further optimized the adsorption parameters using the pH of the solution, the initial concentration, the dose of adsorbent, the temperature, and the contact time. The adsorption kinetics, isotherms, and adsorbent regeneration were also evaluated to determine the adsorption nature and reusability study.

2. Materials and methods

2.1. Materials

The chemicals such as $Fe(NO_3)_3{\cdot}9H_2O$ (≥98.0%), $Zn(NO_3)_2{\cdot}6H_2O$ (≥99.0%),$Ni(NO_3)_2{\cdot}6H_2O$ (≥99.0%) and $Cd(NO_3)_2{\cdot}4H_2O$(≥99.0%) were purchased from Sigma-Aldrich. The reagents were used in their

purest form. Distilled water was used to prepare the solutions. The pinecone biomass used to produce biochar was collected from Andries Potgieter Boulevard, Vanderbijlpark Gauteng province in South Africa. Pyrolysis was performed in a laboratory at the School of Science, Engineering, and Technology of the University of Florida of Science and Technology in Johannesburg.

2.2. Synthesis of ZNiF@PB

ZNiF@PB was synthesized using a method optimized and described by Masuku et al. (2024). Briefly, ZNiF@PB was synthesized by combining two-step synthesis methods. First, pinecone biomass was ground to smaller sizes and pyrolyzed at a temperature of 525 °C in a muffle furnace for 180 min at a heating rate of 6 °C/min that was cooled under ambient conditions for 120 min in a desiccator (Masuku et al., 2024). The coprecipitation synthesis of ZNiF was performed by dissolving $Ni(NO_3)_2/Zn(NO_3)_2$ and $Fe(NO_3)_3$ (mole ratio, 1:2) in distilled water (100 mL). Under robust stirring and heating (80 °C), NaOH (2 M) was added dropwise to the metal solution to achieve pH 11. Then the blackish-coloured precipitate formed was washed and dried repeatedly at 105 °C for 12 h. The black powder was called ZNiF and was calcined (180 min at 500 °C at a rate of 5 °C/min) (Masuku et al., 2024). Therefore, ZNiF@PB was prepared by combining PB and ZNiF and dissolving them in 50 ml of distilled water. This solution of ZNiF@PB was heated to 80 °C while stirring for 30 min. Distilled water and ethanol were used to recurrently wash the precipitate formed, which was later dried under conditions similar to those of ZNiF.

2.3. Adsorbent characterization

The properties of the ZNiF, PB, and ZNiF@PB adsorbents are key factors for adsorption studies. Therefore, analytical techniques were used to determine the physicochemical properties of the adsorbent under investigation. Fourier transform infrared (FTIR) (PerkinElmer, Germany) within wavelength ranges of 4000 cm^{-1} to 400 cm^{-1} to identify the chemical functional group of ZNiF, PB, and ZNiF@PB (Masuku et al., 2024). Before analysis, the KBr pellet procedure reported by Masuku et al. (21) was used. The Raman spectrometer was used to determine the rotation of vibration modes of the D and G bands of the adsorbents using a WITec Raman spectrometer (Alpha 300, TS 150) GmbH, Germany. The magnification of this Raman spectrometer analysis was 100× with a laser power of 532 nm (Mmelesi et al., 2022). Brunauer Emmett Teller (BET) calculated the surface area of ZNiF, PB, and ZNiF@PB using Quantachrome Autosorb-iQ, Anton Paar GmbH, Graz, Austria (Mokubung et al., 2024). The crystallinity of ZNiF, PB, and ZNiF@PB was determined using a Rigaku Smart Lab (XRD) X-ray diffractometer from Japan ($\lambda = 0.154$ nm, $2\theta = 20–80°$(Cu – Kα radiation) (Mokubung et al., 2024). A thermogravimetric study (TGA) was used to determine the thermal stability of ZNiF, PB, and ZNiF @ PB (Masuku et al., 2024). The thermal evaluation was carried out in an inert environment using the instrument TGA 5500 (TA Discovery) at 10 °C/min (Mmelesi et al., 2023). Scanning electron microscopy (SEM) and elemental analysis (EDS) were used to examine the surface morphologies of ZNiF, PB, and ZNiF@PB and the elemental compositions, respectively (Masuku et al., 2024). SEM (JEOL JSM − 7800F) coupled with a Thermo Scientific Ultradry EDS detector (Japan) was used for this analysis (Masuku et al., 2024). It should be noted that the samples before analysis were coated with gold and that was done to improve their surface conductivity (Masuku et al., 2024). High-resolution transmission electron microscopy (HRTEM, A JEOL JEM 2100, Japan) provided details on the morphology of ZNiF, PB, and ZNiF@PB (Mmelesi et al., 2023; Mokubung et al., 2024). X-ray photoelectron spectroscopy (XPS, VG ESCALAB MARK II, UK) provided the surface chemical oxidation state of ZNiF, PB, and ZNiF@PB (Mmelesi et al., 2022). Finally, the study of pH at the point of zero charge (pHpzc) was carried out using the solid addition method reported in the literature (Masuku et al., 2024).

2.4. Adsorption experiments

The removal of Cd (II) ions by ZNiF, PB, and ZNiF@PB adsorbent experiments were performed at the University of South Africa (UNISA, Florida Science Campus laboratories). To effectively remove the target pollutant in wastewater, optimizing adsorption parameters becomes very important in adsorption studies. Therefore, several tests were perfomed to determine the sorption conditions in a shaker (250 rpm), using 50 mL of the solution with the initial concentration of Cd (II) between 10 and 150 mg/L and the dose of ZNiF, PB, and ZNiF@PB between 0.05 and 1.0 g/50 mL, the solution pH between 2 and 9, contact time between 20 and 120 min and adsorption temperature at 25–55 °C Using a pH meter, the desired pH of the solution for the adsorption runs was adjusted by 0.1 M of NaOH or HCl solutions. After the adsorption experiment was completed, a Whatman filter membrane paper was used to filter the spent solids (ZNiF, PB, and ZNiF@PB) (Mokubung et al., 2024). NexIONTM 350D, PerkinElmer inductively coupled plasma mass spectrometry (SA (Pty) Ltd) was used to determine the remaining concentration of Cd (II). To calculate the percentage removal efficiency (%) and the adsorption capacity (mg/g), the study used Equations (1) and (2) respectively (Mokubung et al., 2024).

$$\%\ Removal = \left(\frac{Co - Ce}{Co}\right) x100 \tag{1}$$

where Co and Ce are the initial and equilibrium concentrations, respectively (mg/L), the adsorption capacity, qe (mg/g) was also calculated by Equation (2) as the amount of Cd (II) adsorbed by a gram of ZNiF, PB, and ZNiF@PB as an adsorbent under equilibrium conditions.

$$q = \left(\frac{Co - Ce}{m}\right) V \tag{2}$$

where m is the amount of ZNiF, PB, and ZNiF@PB in grams (g), and V is the volume of the Cd (II) solution in liters (L)

2.5. Adsorption isotherms

To better understand the nature of the adsorption mechanism, the study used the Langmuir, Freundlich, and Dubinin-Radushkovich isotherms (D-R) (Llewellyn et al., 2021). The Langmuir isotherm model assumes that adsorption onto the adsorbent occurs through the monolayer, whereas the model of Freundlich's isotherm on the other sides predicts adsorption onto the adsorbent on multilayer and heterogeneous sites. The Dubinin–Radushkovich theory presumes that the adsorption process involves heterogeneous systems. Specifically, it focuses on the adsorption energy following the porosity of the characteristic adsorbent (Masuku et al., 2024). Therefore, the obtained sorption isotherm data were modeled with Freundlich, Langmuir, and Dubinin-Radushkevish isotherm models, as illustrated in equations (3)–(5), respectively (Llewellyn et al., 2021; Niu et al., 2020).

$$q_e = \frac{q_m K_a C_e}{1 + K_a C_e} \tag{3}$$

$$q_e = K_F C_e^{1/n} \tag{4}$$

$$q_e = q_s \exp\left(-\beta \varepsilon^2\right) \tag{5}$$

where qe (mg/g) denotes the adsorption capacity of the Cd adsorbate at equilibrium, qm (mg/g) for the maximum adsorption capacity, Ce (mg/L) is the concentration of the Cd ion at equilibrium, Ka (mg/L) represents the Langmuir coefficient, KF (mg/g) is the Freundlich constants associated with the adsorption capacity, n is the parameter of the adsorption intensity parameter, β (KJ/mol) is the adsorption energy and (K/mol) is the Polanyi potential of the D-R isotherm (Llewellyn et al.,

2021; Niu et al., 2020)

2.6. Thermodynamic studies

To better understand the uptake of Cd (II) ions onto ZNiF, PB, and ZNiF@PB adsorbents, thermodynamics studies were investigated. These parameters examined were the change in (1) free energy, (2) change in entropy, and (3) enthalpy presented as (ΔG: kJ/mol), (ΔS: J/molK))) and (ΔH kJ/mol), respectively. Equations (6) and (7) were used to express these parameters of ΔG, ΔS, and ΔH (Masuku et al., 2024).

$$\Delta G = -RTln\,K_b \tag{6}$$

$$ln\,K_b = -\frac{\Delta G}{RT} = -\frac{\Delta H}{RT} + \frac{\Delta S}{R} \text{ and } \Delta G = \Delta H - T\Delta S \tag{7}$$

Where Kb is calculated from the ratio of Cd (II) on the surface of ZNiF, PB and ZNiF@PB in equilibrium with Cd (II) remaining in the solution, ΔS for the change in entropy (J/molK, (°C), ΔH for the change in enthalpy (kJ/mol) calculated from the slope and intercept of ΔG versus 1/T and R represents the ideal gas constant (8.314 J/mol K), T correlates with the temperature.

2.7. Adsorption kinetics

Adsorption experiments were used to investigate kinetic studies using the initial concentration of Cd (II) metal, and this was carried out at different contact times from 20 to 120 min. Many kinetics models have been reported in research, but the use of pseudo-first order (PFO), pseudo-second-order (PSO), and intraparticle diffusion (IPD) models has proven effective for heavy metal uptake by spinel ferrite and their corresponding nanocomposites (Masuku et al., 2024; Singh et al., 2023). Equations (8)–(10) explain the kinetic models of PFO, PSO, and intraparticle diffusion (IPD), respectively.

$$q_t = q_e\left(1 - e^{-kt}\right) \tag{8}$$

$$q_t = \frac{k_2 q_e^2 t}{1 + k_2 q_e t} \tag{9}$$

$$q_t = k_i t^{0.5} + C \tag{10}$$

where for PFO and PSO, qe and qt (mg/g) are the amount adsorbed at equilibrium, and t is the time and k1 constants of the model rates (min^{-1}) and k_2 (g/mg min). For IPD, qt is the adsorption capacity (mg/g) at equilibrium and ki is the IPD rate constant, while C is the intercept of the sorption capacity at time versus the square root of time.

2.8. Reusability of the absorbent

Repetitive reuse of the prepared ZNiF, PB, and ZNiF@PB adsorbents can successfully mitigate the costs of the adsorbents and their disposal costs, which is very important in wastewater treatment plants. For this work, consecutive runs under optimal conditions such as pH, adsorbent mass, temperature, and initial adsorbate concentration (pH: 6.0, m: 0.5g/50 mL, T: 25 (°C) and Co: 100 mg/L and t: 120 min) were contacted with 0.5g/50 mL of the three adsorbents in a series of adsorption experiments. After adsorption, the solutions were filtered and the filtrate was measured, while the ZNiF, PB, and ZNiF@PB samples were recovered from the reaction mixture using the centrifugal method. The adsorbents were dried at 105 °C in the oven for 12 h. Subsequently, the desorption of the ZNiF, PB, and ZNiF@PB material was performed using NaOH and HCl solutions to remove the cadmium ion. The adsorption/desorption studies were performed for five sequential reaction cycles, which were all conducted under the same experimental circumstances.

3. Results and discussion

3.1. Adsorbent characteristics

3.1.1. FTIR spectrum

To categorize the different functional groups of ZNiF, PB, and ZNiF@PB and to better understand the various bonding interactions within the nanocomposite, the study used FTIR spectrometry in the range of 400 and 4000 cm^{-1}. Fig. 1 presents the results. The important peaks that described the ZNiF spinel ferrites were the stretching vibration of OH due to adsorbed water on the ZNiF surface between the frequency of 3454 and 1640 cm^{-1} (Hu et al., 2022; Sahoo et al., 2021). Between 592 and 653 cm^{-1} were the ν_1 and ν_2 bands respectively confirming metal oxygen at the octahedral and tetrahedral sites (Dave and Sirach, 2023; Mangood et al., 2023). The peak at 1110 cm^{-1} was due to adsorbed molecules of carbon dioxide molecules (Naik et al., 2023). PB showed a peak of stretching vibration at 3438 cm^{-1} which was due to the hydroxyl groups (OH), phenols, and monomeric alcohol (Adeniyi et al., 2023; Sharma et al., 2023). The starching frequencies at 2369 and 2339 cm^{-1} correspond to H and C = C, respectively (Liu et al., 2019). The carbonyl (C=O) functional group of ketones, amides, and aldehydes occurred at 1638 cm^{-1} while the aromatic hydroxyl/carboxylic (COOH) was achieved at 1385 cm^{-1}. The PB also had a shoulder of 1009 cm-1 which represents the primary alcohol group (CO) (Hassaan et al., 2023). Finally, the peaks of cellulose, lignin, and hemicellulose (C-O-C) occurred in the 1124 cm^{-1} region (Hassaan et al., 2023). For the ZNiF@PB nanocomposite FTIR spectra, the presence of the peaks at 756 cm^{-1} (Fe-OH) and 512 cm^{-1} (Fe-O/M-O) along with other common peaks of PB observed in the figure confirmed the incorporation of PB into $NiZnFe_2O_4$.

3.1.2. The Raman spectrum

The Raman spectrometer provides details on the structural properties of the prepared ZNiF, PB, and ZNiF@PB materials. The investigations were carried out at ambient temperatures in a wavelength range of 0–4000 cm^{-1}. Fig. 2 shows the results of PB, ZNiF, and ZNiF@PB. For ZNiF nanoparticles, four bands were observed in Eg, T2g (2), T2 g(3), and A1g corresponding to Raman shifts of 315, 474, 554, and 683 cm^{-1}, respectively. The possible explanation for the existence of these bands at wavenumbers 315, 474, 554, and 683 cm^{-1} was due to the symmetric bending of the O_2 anions from AO_4 (tetrahedral units) and O_2 atoms at the Fe^{3+} octahedral sites (FeO_6), attributed to the

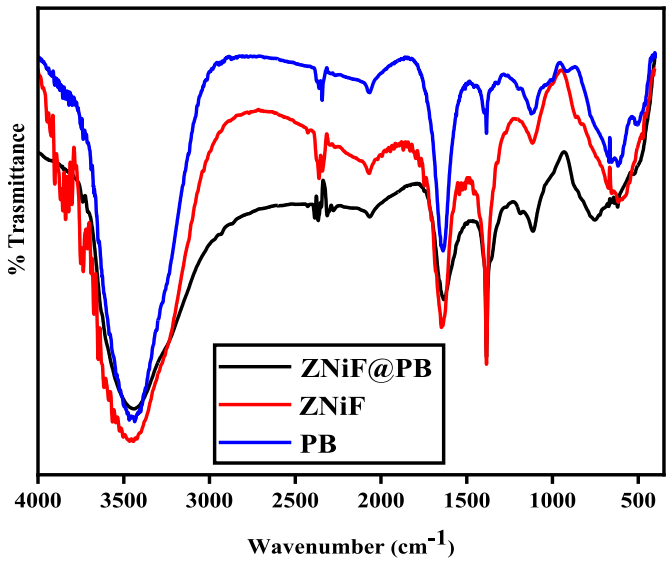

Fig. 1. FTIR spectrum of ZNiF, PB, and ZNiF@PB to indicate the presence of the functional groups.

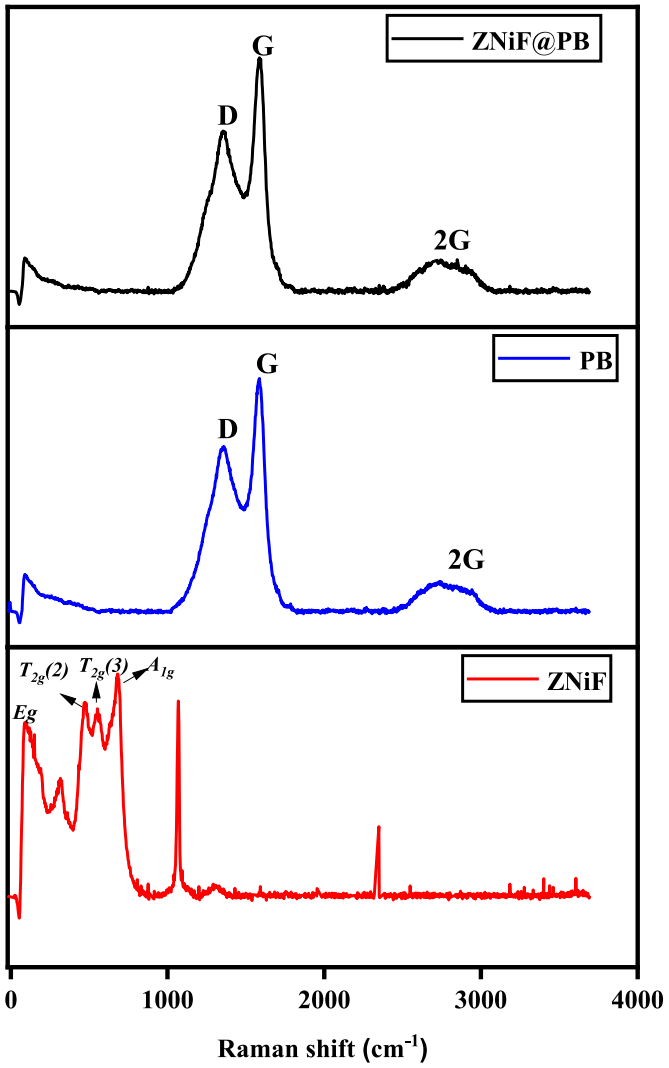

Fig. 2. Raman spectrum of ZNiF, PB, and ZNiF@PB.

asymmetric bending of coordinated O_2 to Ni^{2+} occurring at the octahedral sites, and the mode due to symmetric breathing (FeO_4), respectively (Song et al., 2023). For the Raman shift greater than 500 cm^{-1} (tetrahedral sublattices), the band had three slit energy levels Ni-O (541 cm^{-1}), Zn-O (554 cm^{-1}), and Fe-O (660 cm^{-1}). Therefore, this phenomenon implies that Ni, Zn, and Fe occupy the tetrahedral A sites. It was also noted that the relative area of the three peaks found in this work differed from that previously reported in literature studies, which could be explained by the choice of synthesis method (coprecipitation) that influences the cation distribution (Palacio Gómez et al., 2020). Previously, conducted works reported spinels with a small peak at 189 cm^{-1} for T2g (Song et al., 2023) yet, for the present work, that peak was out of range and cannot be reported. In the absence of T2g, the result of the Raman analysis was comparable to previously reported spinel ferrite. Therefore, it can be confirmed that the ZNiF nanoparticles had a cubic structure without the impurity phase of the α-Fe_2O_3 phase at 240–300 cm^{-1} (Bashar et al., 2023; Cheng et al., 2023; Mmelesi et al., 2022; Palacio Gómez et al., 2020). For the PBC Raman analysis, there are three peaks, where two peaks are sharp clumps of the D band with an intensity of 1360 cm^{-1} and the G band with an intensity of 1586 cm^{-1}. The Disorder in the D band is correlated with A1g vibrational modes caused by defects in the graphitic layers, and these imperfections in the structure of the PB are the result of the high percentage of carbon in the biochar (Eshun et al., 2019). However, the result of the G disorder was attributed to sp2 crystallite vibrations of carbon atoms in graphitic material (Bai et al., 2023; Cheng et al., 2023; Guo et al., 2019). Previous research on Raman shifts from biochar materials described the appearance of a G disorder as a result of the aromatic ring of biochar (Eshun et al., 2019; Patel et al., 2023). Similarly, others have presented that the G bond is an E2g symmetry vibration of the graphite lattice, indicating a degree of charge transfer (Ali et al., 2023; Chia et al., 2012; Eshun et al., 2019; Li et al., 2023; Sadezky et al., 2005). The synthesized ZNiF@PB had two prominent peaks observed at 1359 cm^{-1} (D band) and 1585 cm^{-1} (G band) attributed to sp2 vibration modes of sp2 of defective carbon structure and carbon atoms of sp2 in graphite layers. At around the wavenumber 2827 cm^{-1}, the ZNiF@PB further illustrates that there was a broad and weak peak due to the stacking order of the carbon structures (Masuku et al., 2024). The degree of graphitization, crystallinity of the carbon material, and defect density of the ID/IG ratio, which are derived from the intensity of the D and G bands, were also calculated. ZNiF@PB had a higher (I_D/I_G) (0.87) than that for PB (0.86) showing that with the coprecipitation method, there was slightly more formation of disordered defects within the structure of the PB.

3.1.3. BET surface area

The adsorption-desorption isotherms of the prepared ZNIF, PB, and ZNiF@PB materials were investigated to calculate the surface area, the pore size, and the pore volume (Masuku et al., 2024). The experimental temperature was −196 °C and all experiments were carried out in an inert atmosphere. N2 adsorption-desorption isotherms exist in various types according to their shapes, the first (I) is Henry, the second (II) is Langmuir, the third (III) is Freundlich, the fourth (IV) is BET, and the fifth (V) is stepped type. Three groups are used to explain the porosity of the sample,>2 nm (microporous) 2–50 nm (mesoporous), and >50 nm (microporous) (Xia et al., 2024). As observed in Fig. 3, clearly all samples exhibited a type IV isotherm, which means that the materials were mesoporous. The isotherms obtained correlate with the classification of the International Union for Pure and Applied Chemistry (IUPAC) (Masuku et al., 2023a). ZNiF had two hysteresis loops observed with a rise in relative pressure at 0.2 to 0.8 and 0.8 to 1.0 and these results were attributable to the fact that during synthesis the spinel ferrite became agglomerated, thus resulting in particles with a broader pore size of micropores and mesopores. Therefore, the estimated surface area, pore size, and pore volume of ZNiF were 78.4 m^2/g, 14.9 nm, and 0.34 cm^3/g. For the PBC material, mesoporous and micropore structures were observed and the calculated surface area, pore size, and pore volume were 125 m^2/g, 1.4 nm, and 0.07 cm^3/g. For the ZNiF@PB isotherm, the nanocomposite still achieved its mesoporous nature with a surface area of 104 m^2/g, a pore size of 3.41 nm, and a pore volume of 0.12 cm^3/g. When comparing the structural pore properties of the ZNiF, PB, and ZNiF@PB materials, it was anticipated that due to the porous nature of pinecone, the BET surface area of biochar 125 m^2/g would be high, allowing Pb to be an effective carrier for the growth of nanoparticles (Liang et al., 2024).). However, the growth of ZNiF nanoparticles resulted in a slight decrease in the surface area of ZNiF@PB of 104 m^2/g and its surface area was still greater than that of pure ZNiF of 78.4 m^2/g, implying that the PB carrier is helpful in the dispersion of ZNiF. The higher surface area of the ZNiF@PB nanocomposite compared to that of the ZNiF nanoparticles is important for the enhancement of the adsorption sites for the removal of cadmium ions from wastewater. Similarly, the pore size of the nanocomposite was larger; therefore, it was more beneficial to adsorb cadmium ions than PB (Liang et al., 2024). The table summarizes the textural properties of the prepared samples.

3.1.4. XRD analysis

The crystalline phases of the prepared PB, ZNiF, and ZNiF@PB adsorbents were determined using an X-ray diffractometer (XRD), and the results are shown in Fig. 4. The PB XRD pattern presents common peaks belonging to graphite microcrystals 2θ = 10°, 23° and 43° (Yuan et al., 2024). The XRD results show that PB had an amorphous structure due to

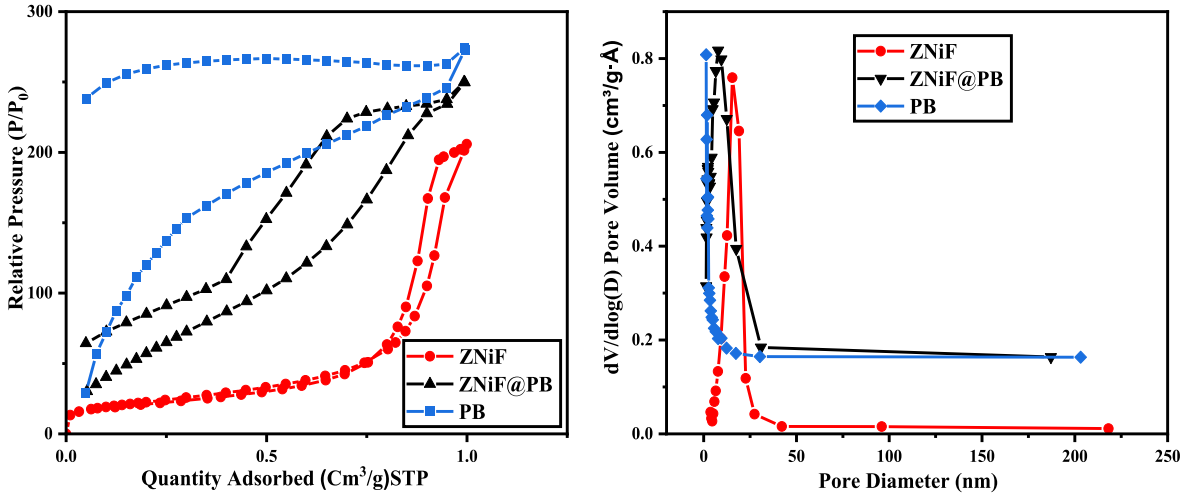

Fig. 3. Adsorption-desorption isotherms of ZNiF, PB, and ZNiF@PB.

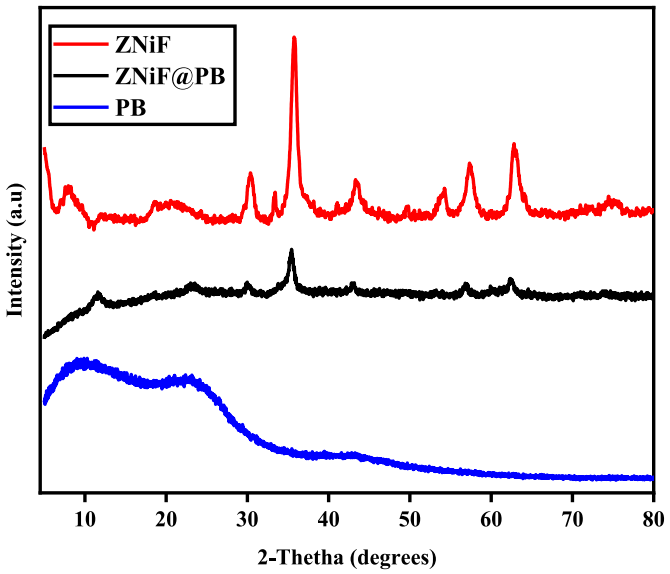

Fig. 4. Xrd of ZNiF, PB, and ZNiF@PB.

its lignocellulosic biomass with crystalline particles (Khan et al., 2023). The results obtained are comparable with those of the work by Khan et al. showing a peak of cellulose crystallite at 22.6° (Khan et al., 2023). The ray diffraction structure of the prepared ZNiF nanoparticle reveals peaks of 30°, 36°, 43°, 54°, 57° and 63° correlating to crystalline planes with indices (220), (311), (400), (422), (511) and (440), respectively. The ZNiF nanoparticle XRD pattern matches the card number (JCPDS card number 89–4927) (Manohar et al., 2023). The ZNiF nanoparticle diffraction peaks showed high crystallinity (sharp and intense peaks), confirming the inverse cubic spinel structure with no impurity peaks observed (Manohar et al., 2023). The diffraction spectrum of ZNiF@PB shows that ZNiF and PB peaks are present on the nanocomposite surface (ZNiF@PB). The nanocomposite inherits 2θ characteristics peaks at 12°, 19°, 23°, 30°, 36°, 43°, 54°, 57°, and 63° attributed to the miller indices (111) (220), (311), (400), (422), (511) and (440) (Khan et al., 2023; Shoukat et al., 2021). The diffraction peaks attributed to PB in the structure ZNiF@PB were those at 12°, 19°, and 23°, indicating that the biochar was successfully loaded onto spinel ferrite (Hu et al., 2022; Yuan et al., 2024). Looking at the XRD patterns of the uncoated ZNiF and those of the ZNiF@PB, similar peaks were observed; however, the difference was in their peak strengths, where the ZNIF@PB peaks were slightly reduced due to the amorphous PB on the ZNiF surface (Hu et al., 2022). The Derby-Scherrer equation was used to calculate the crystallite size of the three materials using the highest peak of 311. The D stands for particle diameter, K is the Scherrer constant at 0.94, λ is the wavelength given by 1.541 Å, β for the full-width at half maximum (FWHM), and θ correspond to the angle of incidence (Masuku et al., 2024).

$$D = \frac{K\lambda}{\beta \cos\theta} \tag{12}$$

The crystallite sizes of ZNiF, PB, and ZNiF@PB were 43 nm and 38 nm, respectively. The decrease in the crystallite size of ZNiF@PB implies the successful biding and the presence of PB on the spinel ferrite surface (Masuku et al., 2024).

3.1.5. TGA analysis

The study investigated the thermal stability of ZNiF, PB, and ZNiF@PB materials by thermogravimetric analysis. During the experimental procedure, the heating temperature was investigated from 30 to 900 °C in an inert environment. Fig. 5 illustrates the thermal stabilities of the three materials that exhibited degradation in three phases. For ZNiF nanoparticles, the primary step below 200 °C accounts for moisture loss and NaOH removal on the surface of spinel ferrite (Chakhtouna

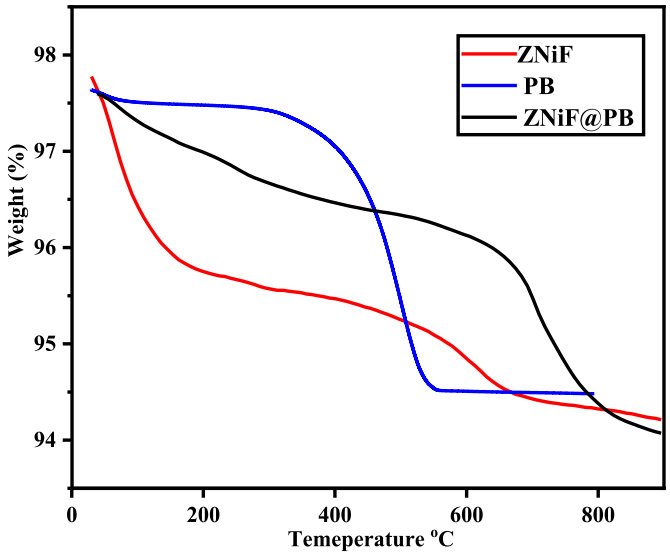

Fig. 5. TGA of ZNiF, PB, and ZNiF@PB.

et al., 2021). The second decomposition between the temperature of 31–184 °C was attributed to chemicals absorbed during ferrite preparation, the breakdown of the ZNiF complex (Xia et al., 2024). The third degradation step at temperatures of 519–646 °C and 642–681 °C was due to the loss of the metal-oxygen bond (Belaiche et al., 2022; Xia et al., 2024). Usually, complete thermal decomposition of spinel ferrite nanoparticles occurs at a temperature of less than 700 °C , and the results of the current study agree with the previous thermal stability curve of spinel ferrites (Belaiche et al., 2022; Hong et al., 2020). For the PB sample, the initial step correlates with the loss of adsorbed water, volatiles, and carbon dioxide and was achieved at a temperature below 100 °C (Peng et al., 2021). The PB also showed its second degradation phase between a temperature of 100 and 315 °C. At this stage, there was a dissociation of cellulose and hemicelluloses in the form of NH_3, CO_2, and H_2O (Amen et al., 2020; Peng et al., 2021). Char formation in the third stage occurred between temperatures 531 and 550 °C; beyond 550 °C, little degradation occurred, which means that the process was complete. For the ZNiF@PB nanocomposite, the first step below 200 °C corresponds to the loss of water and volatiles (Peng et al., 2021). The second thermal decomposition stage between 242 and 431 °C was the result of the conversion of cellulose, lignin, and hemicellulose from PB to H_2O, CO_2, C, and NH_3 (Peng et al., 2021; Xia et al., 2024). This TGA curve observed in the range of 431–665 °C was attributable to the degradation of cellulose and lignin and the oxidation of ZnO, NiO, and Fe_2O_3. However, studies by Li et al. attributed this degradation step as a confirmation that PB molecules were strongly attached to ZNiF nanoparticles (Li et al., 2020). The fourth degradation step that occurred above 665 °C was due to spinel ferrite and graphitized carbon (Peng et al., 2021; Xia et al., 2024). Based on the temperature used for the carbonization of PB and the crystallization temperature of ZNiF, the pyrolysis temperature of the synthesized ZNiF@PB was within the range of 550 °C.

3.1.6. SEM analysis

The analysis was performed for the morphological structure of ZNiF, PB, and ZNiF@PB, and the results of the chemical composition are shown in Fig. 6 (a), respectively. The SEM image in Fig. 6a indicates ZNiF micrographs showing irregular structure and particle aggregation (Fito and Nkambule, 2023; Wani et al., 2023). In addition, the images were shaped like small blocks that looked like quasi-cubic shapes (Dave and Sirach, 2023). On the other hand, Fig. 6b shows that the surface of PB was relatively smooth with a honeycomb-shaped pore structure (Dave and Sirach, 2023). Generally, an adsorbent with a good pore size offers a higher surface area, making it possible for pollutants to absorb easily on the adsorbent surface. After incorporating PB on the surface of the ZNiF nanoparticles, Fig. 6c clearly shows that the surface of the nanocomposite became rougher, confirming more active sites for adsorption and improved pollutant removal (Masuku et al., 2024).

3.1.7. EDX analysis

For the constituent elements of ZNiF present, the study performed an EDX analysis on the prepared nanoparticles. The results in Fig. 7a–c presents the composition of the samples and their KeV on the x-axis. The ZNiF in Fig. 7a is mainly composed of Ni (8.7 KeV), Zn (1.4 KeV), Fe (6.4 KeV), and O (2.8 KeV), and the Wt % of the ZNIF of Ni, Zn, Fe, and O was 19.5 %, 5.2 %, 53.2%, and 22.1 %, respectively. The elements of PB in Fig. 7b and their KeV are C (1.3 KeV), O (1.1 KeV), and K (0.7 KeV). PB also had a Wt % for C, O, and K at 86.6%, 8.8 %, and 4.7%, respectively. The presence of the potassium element was because the sample was plant-based. For the nanocomposite ZNIF@PB sample, the elements were Ni (0.4 KeV), Zn (0.3 KeV), Fe (0.3 KeV) and O (0.8 KeV). The weight percentage of Ni, Zn, Fe, O, and C was 8 %, 0.6 %, 9.4%, 24.4%, and 56.6, respectively.

3.1.8. TEM analysis

TEM analysis provides more information on the structural properties and morphologies of the samples. Fig. 8a and b illustrate micrographs of pure ZNiF (a) and ZNiF@PB nanocomposite (b) samples synthesized using the coprecipitation method. As observed, both samples showed that the particles were almost spherical and had different particle sizes.

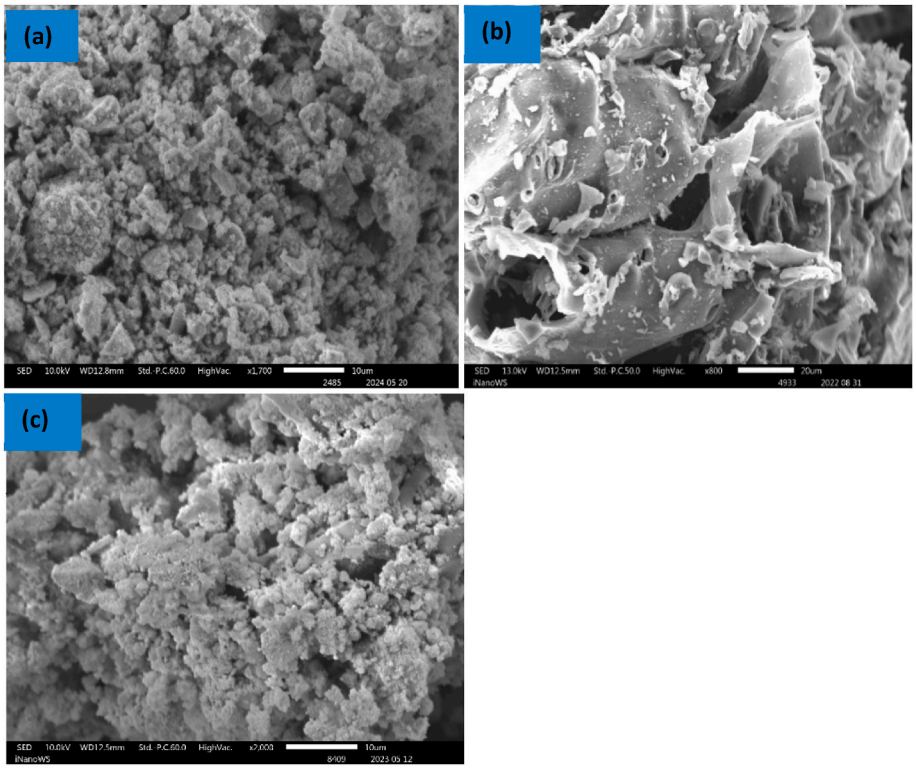

Fig. 6. SEM images of ZNiF (a), PB (b), and ZNiF@PB (c).

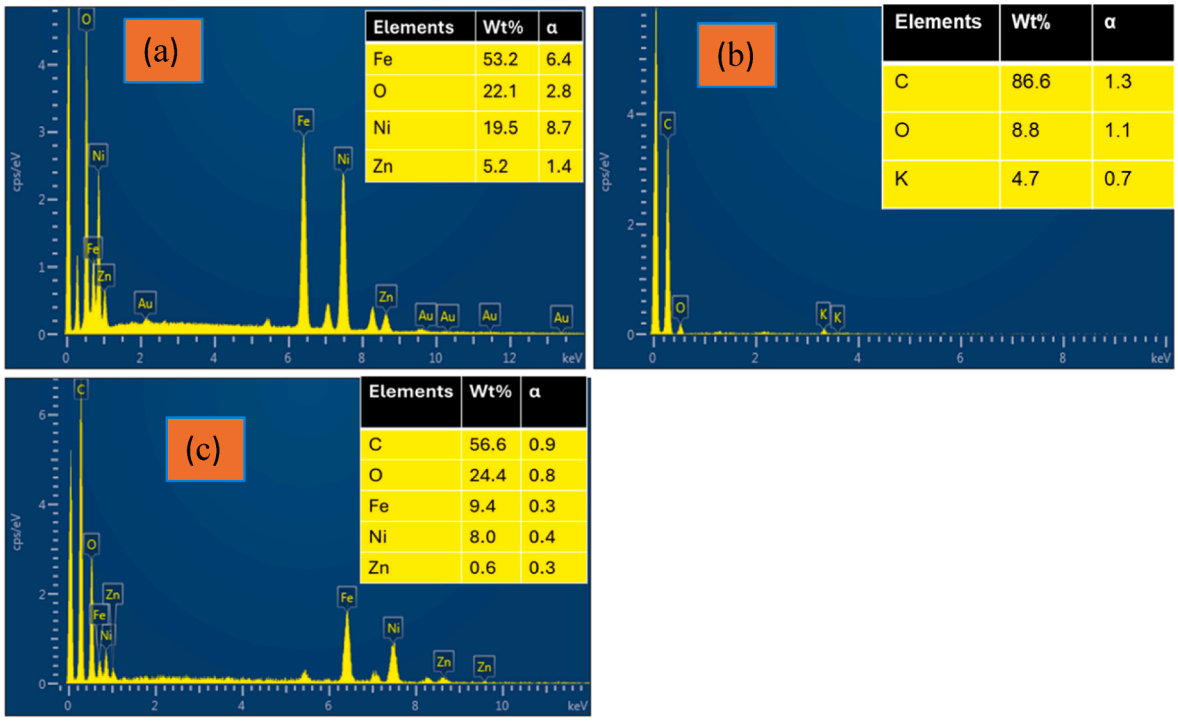

Fig. 7. EDX analysis of ZNiF, PB, and ZNiF@PB.

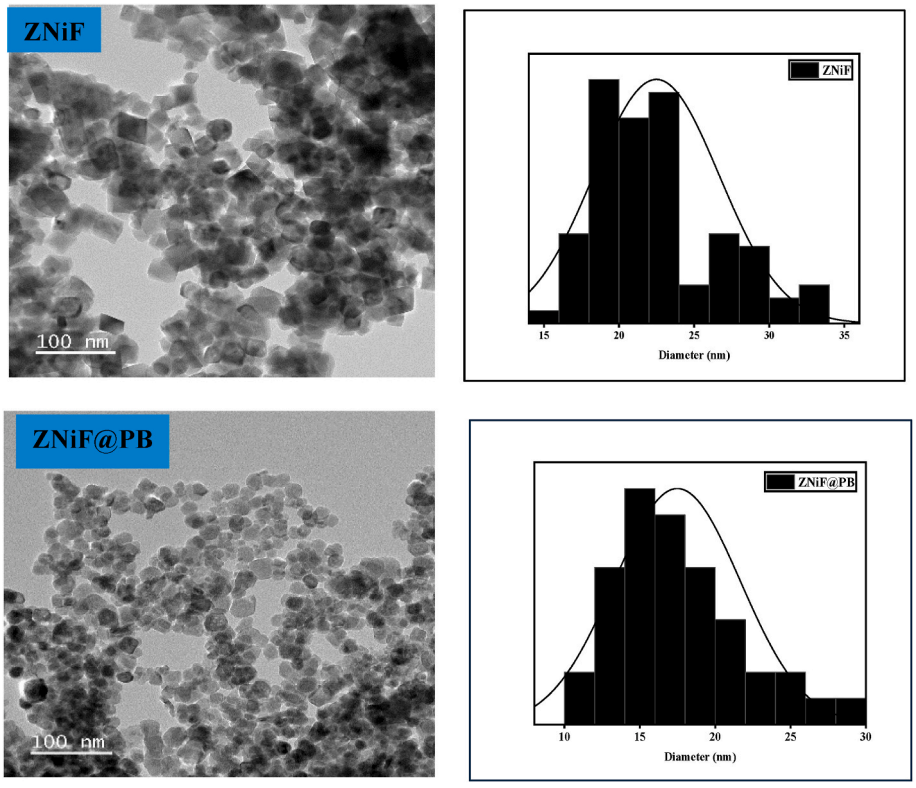

Fig. 8. TEM images of the structural properties of ZNiF and ZNiF@PB.

However, ZNiF nanoparticles show a slight agglomeration of the particles due to their magnetic characteristics between the nanoparticles and high surface energies (van Der Waals forces), or it could be due to the adopted synthesis method (Mapossa et al., 2020; Wani et al., 2023). However, the particles of the nanocomposite (ZNiF@PB) separated better than those of the bare ZNiF and this could be ascribed to the precipitation of ZNiF nanoparticles onto PB. Therefore, there was an interaction between the surface groups of ZNiF and the surface of PB, which in turn controls the growth of the particles by lowering the surface energies of the particles, resulting in a lower level of aggregation.

Similarly, the PB functional groups fine-tuned the surface of the ZNiF nanoparticles, causing a reduction in the particle size of the material. The size measurements exhibited for the ZNiF and ZNiF@PB nanoparticles were 23 ± 0.5 nm and 18 ± 0.5 nm, respectively.

3.1.9. XPS analysis

To determine the ZNiF nanoparticles and the surface chemical state of the ZNiF@PB nanocomposite, the study employed XPS analysis. Fig. 9 (1) a-e present the XPS results of ZNiF nanoparticles, while Fig. 9(2) a-f illustrate the XPS results of the ZNiF@PB nanocomposite. For the ZNiF

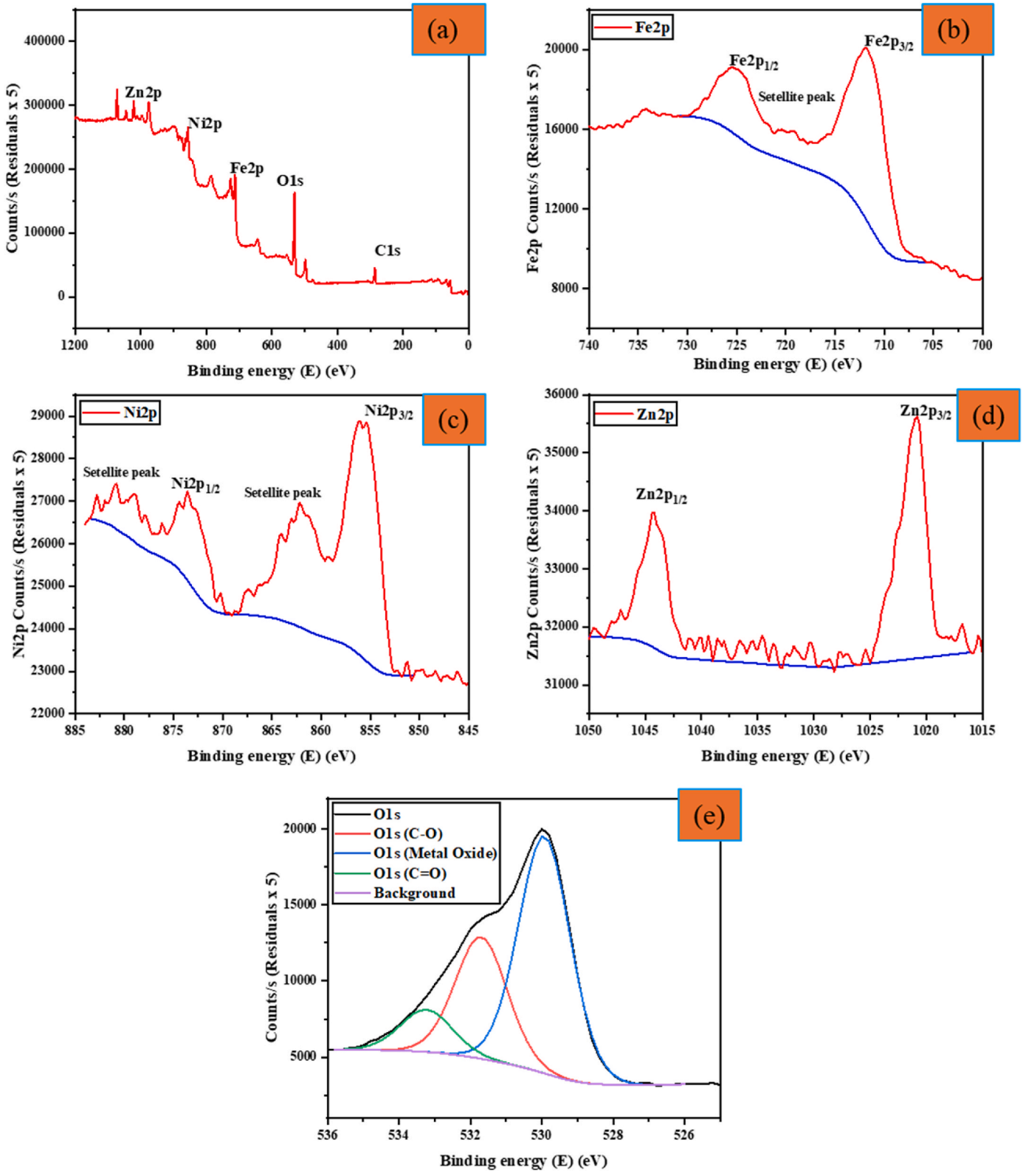

Fig. 9. (1) a-e. XPS spectrum of ZNiF.
Fig. 9(2) a–f: XPS spectrum of ZNiF@PB.

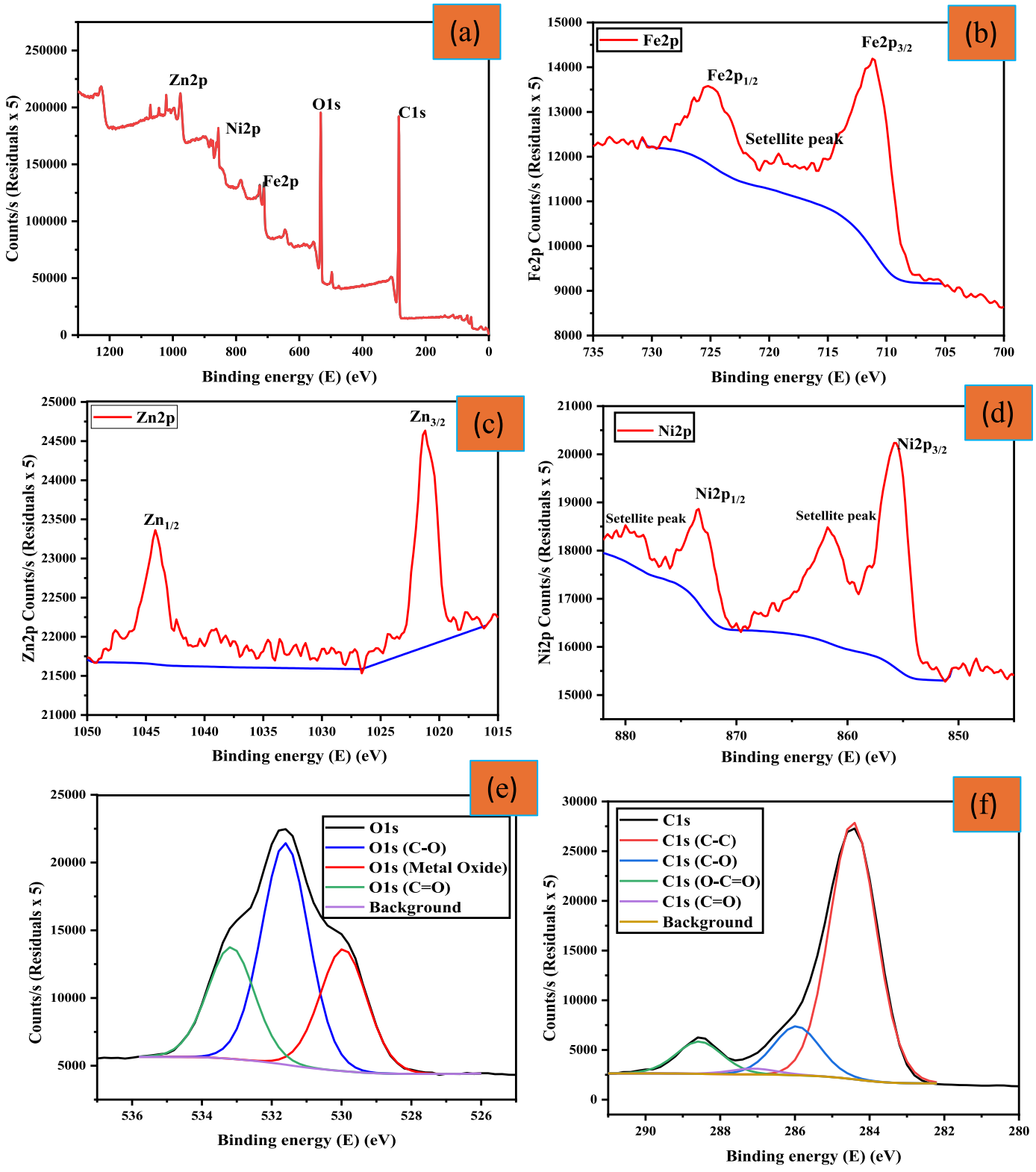

Fig. 9. (*continued*).

nanoparticles in Fig. 9 (1a), the identified core levels were Fe2p, Ni2p, Zn2p, O1s, and C1s. The appearance of C1s could be attributed to adventitious hydrocarbon adsorbed on the surface of nanoparticles (Mmelesi et al., 2022). As observed in Fig. 9(1b), the Fe2p spectrum of Fe2p had three characteristic peaks at 711.2 eV and 725.4 eV for $Fe2p_{3/2}$ and Fe $2p_{1/2}$, respectively. Other small satellite peaks in the Fe2p spectrum appeared at 719.2 eV and 720.3 eV, which indicates that Fe was in the form of Fe^{3+} (trivalent iron) occupying tetrahedral sites (Masuku et al., 2023b; Mmelesi et al., 2022; Yong et al., 2022). For the Ni2p Fig. 9(1c) spectrum, it was evident that there were four characteristic peaks of $Ni2p_{1/2}$ (shake-up satellite), $Ni2p_{1/2}$, $Ni2p_{3/2}$ satellite, and $Ni2p_{3/2}$ at 881.0, 874.0, 862.0, and 856.0 eV, respectively. The existence of Ni $2p_{3/2}$ peaks and satellite peaks in the spectrum shows the presence of divalent nickel ions (Ni^{2+}) (Dhiman et al., 2023). However,

the Zn2p spectrum Fig. 9(1d) shows binding energies at 1021.0 eV for the peak $Zn2p_{3/2}$ and 1044.4 eV for the peak Zn $2p_{1/2}$ which confirms that Zn has an oxidation state (+2) in the material (Mmelesi et al., 2022; Yong et al., 2022). In Fig. 9(1e) three distinct O1s peaks were observed at 533.2, 531.8, and 530.0 eV. The appearance of peaks at these binding energies was the result of adsorptive oxygen (carbon monoxide and carbon dioxide) and species of lattice oxygen (metal oxygen) in $NiFe_2O_4$ nanoparticles (Mmelesi et al., 2022). For the ZNiF@PB nanocomposite in Fig. 9 (2a), the XPS analysis explored the state and chemical composition of the elements where the spectrum identified core levels of Fe2p, Ni2p, Zn2p, O1s, and C1s. The existence of PB was confirmed by the presence of the intense characteristic peak of C1s in the spectra of the ZNiF@PB nanocomposite. The ZNiF@PB shows Fe2p in Fig. 9(2b) with three peaks at 711.0 eV and 720.4 eV for $Fe2p_{3/2}$ and Fe $2p_{1/2}$, respectively. Other observed peaks in the Fe2p spectrum were those attributed to satellite peaks at 719.3 eV and 720.4 eV because Fe occurs in trivalent form Fe^{3+} (Mmelesi et al., 2022; Yong et al., 2022). The spectrum of Fig. 9(2c) for the Ni2p spectrum had four distinct peaks of $Ni2p_{1/2}$, $Ni2p_{1/2}$ (satellite), $Ni2p_{3/2}$, and $Ni2p_{3/2}$ (satellite) at 874.0, 880.1, 856.0, and 862.0 eV, respectively. The satellite peak indicates the existence of Ni2+ ions (Mmelesi et al., 2022). The binding energies of Zn2p shown in Fig. 9(2d) occurred at 1021.2 eV for the $Zn2p_{3/2}$ peak $Zn2p_{3/2}$ and 1044.2 eV for the peak Zn $2p_{1/2}$ peak signifying that Zn has an oxidation state of a +2. The high resolution O1 spectrum in Fig. 9(2e) comprised three clear peaks located at 530.0, 531.6, and 533.2 eV, which were ascribed to Fe-O/Ni–O, C-O, and C = O/O-H, respectively. The results also showed the spectrum of C1s that had peaks at 284.4, 286.6, 288.4, and 287.2 eV which corresponds to the functional groups C–C, C–O, O–C=O, and C = O in the PB matrix, respectively. The previously investigated manganese ferrite coated magnetic biochar composite ($MSMnFe_2O_4$/MBC) observed similar results to this study (Bai et al., 2023; Yong et al., 2022). The XPS results and the elements in the ZNiF and ZNiF@PB samples were consistent with the EDX spectrum results (Fig. 7 which confirmed that the synthesized materials had no impurities.

3.1.10. pHpzc

The adsorption process can be influenced by the properties of the adsorbent in the aqueous solution. Among the characteristics of ZNiF, PB, and ZNiF@PB materials is the point of zero charge (pHpzc), which is important in the adsorption findings. Generally, pHpzc describes the pH point at which the equilibrium concentration occurs between the anionic and cationic surface charges (Masuku et al., 2024). The surface of the synthesized ZNiF, PB, and ZNiF@PB becomes cationic due to protonation when pH < pHpzc which attracts anions. Likewise, if pH > pHpzc the surface is negative for ZNiF, PB, and ZNiF@PB, thus supporting cation adsorption (Fito et al., 2023c; Hashem et al., 2024). In this study, pHpzc was found to be 6.06, 5.90, and 6.46 for ZNiF, PB, and ZNiF@PB, respectively, as illustrated in Fig. 10.

3.2. The influence of adsorption factors on Cd (II) removal

3.2.1. Solution pH of solution

The aqueous pH in the adsorption process governs the surface charge, the dissociation of the functional groups of the active sample, and the speciation of metals (Masuku et al., 2024). Normally, the surface charge of the adsorbent can be altered by changing the solution pH; therefore, it is necessary for these parameters that affect the adsorption processes to be properly optimized for the effective removal of metal ions from the aqueous solution (Fito and Nkambule, 2023; Masuku et al., 2024). To determine the effect of pH on the Cd (II) uptake by the ZNiF, PB, and ZNiF@PB adsorbents, various solutions with pH values between 2 and 12 were investigated. During this time, experimental conditions such as the mass of the adsorbent, the temperature, the initial concentration of the adsorbate, and the time were kept constant (m: 0.1g/50 mL, the temperature: 25 °C, C_o: 100 mg/L and the time: 120 min).

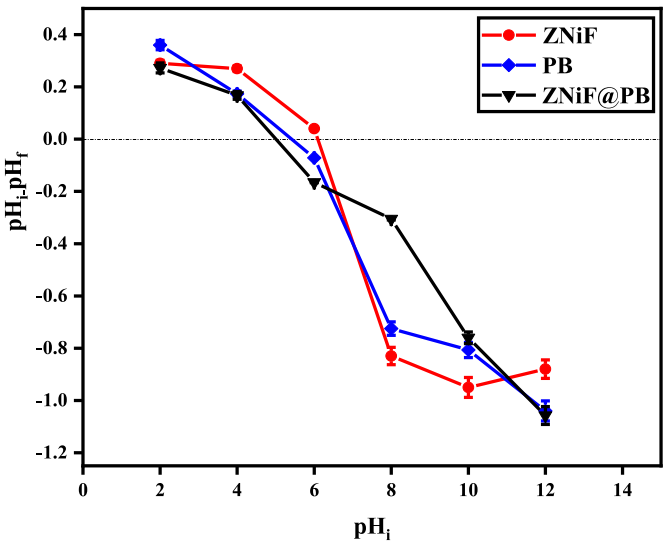

Fig. 10. Influence of pHpzc on the surface charge of ZNiF, PB, and ZNiF@PB under experimental conditions: adsorbent dose 0.1g/50 mL, pH 2 to 12, temperature 25 °C, and contact time: 2880 min.

Fig. 11 presents the results of the pH experiment for all the Cd adsorbent removal percentages (II) that gradually increase with increasing initial pH values. A similar pattern was observed by (Olfatmehr et al., 2022). For PB, the influence of pH arises from the electrostatic interaction between the Cd (II) and PB surface. Moreover, PB has a negatively charged surface, which could favor cationic Cd (II) as the pH increases. Excess protonation of the surface of PB when pH levels were low resulted in charge repulsion between Cd^{2+} and H_3O^+, meaning there was competition for binding. As the pH gradually increased, the PB surface was more negatively charged (deprotonated) because there were fewer hydronium ions in the solution, which indicated that the PB surface has more sorption sites for Cd (II) uptake when the pH of the solution is due to OH ions in the solution. Above pH 6.0, Cd species were reduced with improvement in the formation of soluble Cd-OH^+ (hydroxyl complexes). This shows the difference in PB surface complexes that could be involved in the adsorption process instead of divalent Cd species (Khan et al., 2023; Wu et al., 2019). The Cd (II) crystal structure onto ZNiF nanoparticles shows that the removal efficiency increased with increasing pH. At low pH values and below pH_{PZC}, low Cd (II) removal occurs for two reasons; (1) at these pH values the concentration of H^+ is high, the adsorbent has negative sites to occupy the Cd (II) ions, and then the efficiency is reduced, (2) the positive surface of ZNiF prevents the uptake of Cd (II) cations(Asadi et al., 2020). However, at a pH higher than pHpzc, by reducing the concentration of H^+ and improving the surface negativity of ZNiF due to the ionization groups (–OH– to -O–) that resulted in an increased removal efficiency of Cd (II) cations (Asadi et al., 2020). For the removal of Cd (II) by the ZNiF@PB adsorbent, the results show that at low pH (acidic environment), the adsorption efficiency was low and then gradually increased. This could have happened because, at lower pH, the electrostatic repulsion forces were stronger (competition of H^+ with Cd (II) for active sites) and suppressed the Cd removal (II). In addition, the pH variation can be affected by the behavior of protonation or deprotonation of -OH and -COOH on ZNiF@PB surfaces afterward, affecting the Cd (II) uptake. At low pH, the ZNiF@PB surfaces are positively charged due to surface protonated functional groups. It is difficult for the electropositive ions of Cd (II) to adsorb onto the electropositive surfaces of ZNiF@PB. Therefore, the lower the sorption efficiency. The improved performance with increasing pH was because the surfaces of ZNiF@PB-NH2 move toward more negatively charged as a result of deprotonation of surface functional groups. Thus, the electropositive ions of Cd (II) are more adsorbed by the negatively charged surfaces of ZNiF@PB as a result of

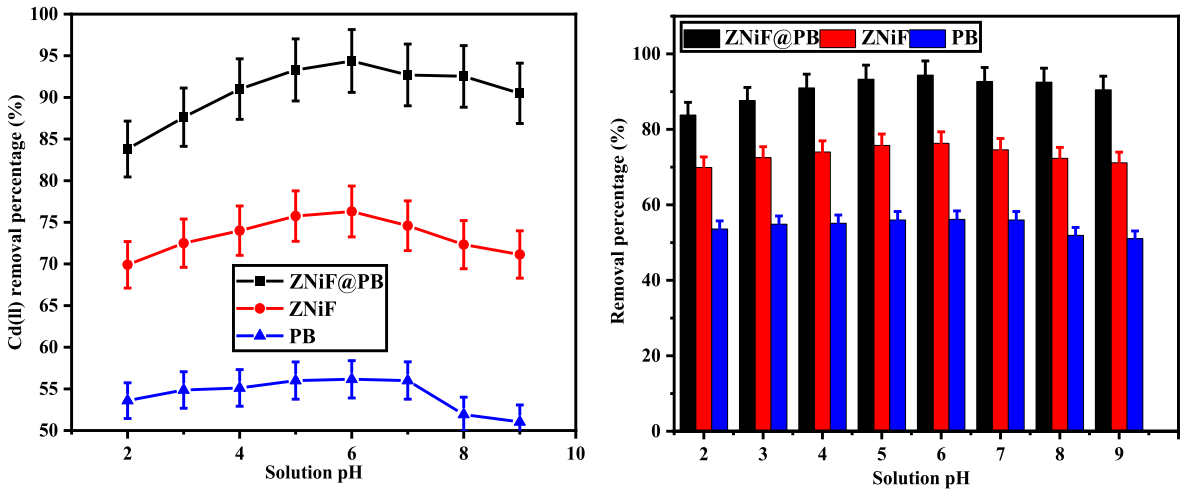

Fig. 11. Influence of pH for Cd (II) on prepared ZNiF, PB, and ZNiF@PB under experimental conditions dosage 0.1g/50 ml, pH 2 to 41, initial Cd concentration 100 mg/L, contact time 120 min and temperature 25 °C.

electrostatic attraction, thereby increasing the adsorption efficiency. For all three adsorbents, it is important to note that Cd (II) forms insoluble hydroxide precipitates when the pH values exceed 6.0, producing a false adsorption efficiency that can affect the accuracy of the experiment. Therefore, we sought to precisely approximate the adsorption of Cd (II) by ZNiF, PB, and ZNiF@PB and to avoid homogeneous Cd (II) precipitation in an aqueous solution. In conclusion, the good sorption efficiency of ZNiF, PB, and ZNiF@PB at a wide range of pH levels proves that all of the adsorbents have potential in environmental wastewater applications for the removal of Cd (II) and possibly other heavy metals. In general, Cd (II) ions were better removed by ZNiF@PB > ZNiF > PB. However, the combined two materials (ZNiF and PB) allow the metal ion to easily be bound on its surface and specific pore structure because of its sizeable surface area, adsorptive sites, and functional groups. In the synergistic process between spinel ferrite and biochar, the biochar serves as anchoring and inhibits the agglomeration of zinc-doped nickel ferrite, thus enhancing the surface chemistry and adsorption performances.

3.2.2. *Adsorbent dose*

The significant parameter for adsorption investigations is the adsorbent dosage. In general, the dose of the adsorbent determines the capacity of the material for the specified concentration of the adsorbate (Masuku et al., 2023b). The experimental procedure for the removal of ZNiF, PB, and ZNiF@PB adsorbents on cadmium ion was performed at various adsorbent masses between 0.05 and 1g. Other experimental values (pH, initial concentration of adsorbate, temperature, and time) were kept constant at pH: 6, Co: 100 mg/L, T: 25 °C, and t: 120 min). Fig. 12 presents the plotted results of the removal efficiency values of Cd (II) versus the dosage of the adsorbent. An increase in the dose of the adsorbent (0.05–1g) increased the efficiency of Cd (II) from 83.1 to 87.0% (ZNiF), 66.3 (PB) to 75.1 and 90.1–96.0% (ZNiF). The increase in removal efficiency arises from the increase in the number of unsaturated adsorbent active sites occupied by Cd (II). When the adsorbent exceeds 0.5g, a considerable change in the Cd (II) ion removal efficiency was observed, because most of the active sorption sites in ZNiF, PB, and ZNiF@PB were now occupied. Therefore, 0.5 g was established as the optimal dose of adsorbents for the efficiency of cadmium removal for all adsorbents and was used in the following experimental procedures. When comparing the three adsorbent adsorption efficiency, the order of the metal ion uptake followed ZNiF@PB > ZNiF > PB and the possible

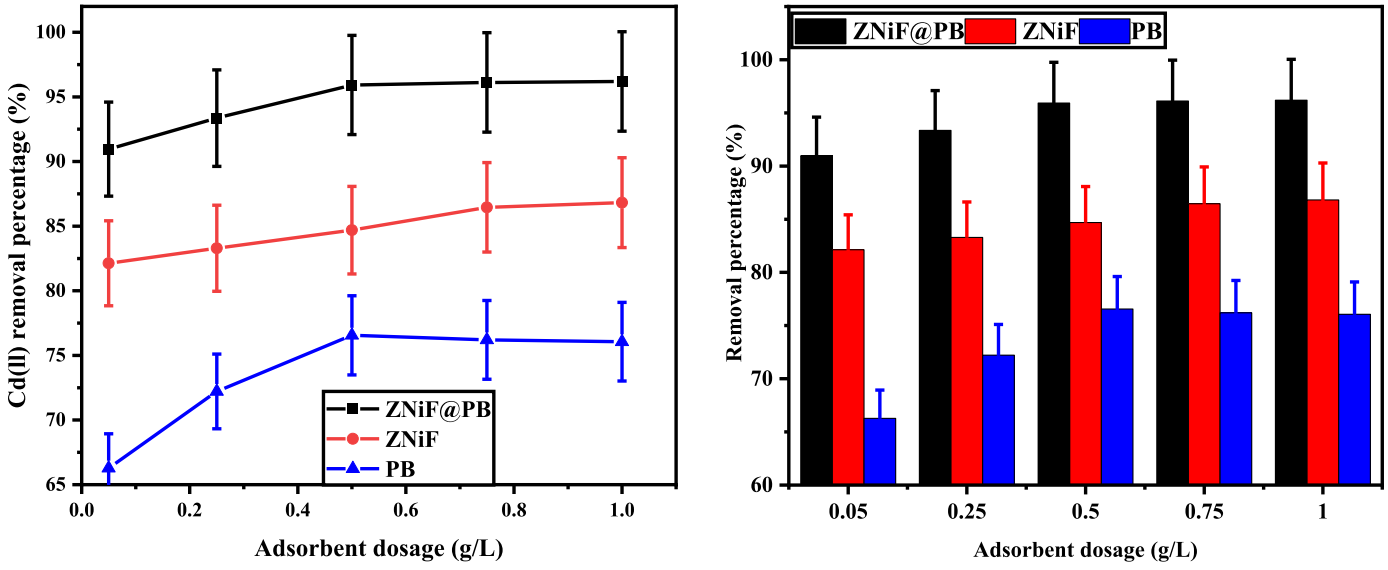

Fig. 12. Influence of the dose of ZNiF, PB, and ZNiF @ PB on the removal of Cd (II) under experimental conditions at solution pH 6.0, adsorbent dose 0.05–1.0 g/50 ml, initial Cd concentration 100 mg/L and contact time 25 °C.

reason for the nanocomposite to have a high removal efficiency could be attributed to the improved surface properties, such as surface area and particle size (Masuku et al., 2024).

3.2.3. Initial Cd concentration

The initial concentration of Cd (II) aims to determine the optimum parameters for the adsorption process. As presented (Fig. 13), the investigations ranged from 10 mg/L to 150 mg/L, while all other experimental values, including pH of the solution, temperature, dose of adsorbent, and time, were kept constant (pH: 6.0, T: 25 °C, m: 0.5g/50 mL and t: 120 min).in). The result in Fig. 13 illustrates a decrease in removal efficiency with an increasing concentration of Cd (II) metal ions. The decrease was from 89 to 73% for ZNiF, 78 to 76% for PB, and 97 to 93% for ZNiF@PB. This result shows that there was a relationship between the Cd concentration and the adsorption efficiency. This can happen at low Cd concentrations; more unoccupied active sites were available, leading to an increase in the uptake of Cd ions by ZNiF, PB, and ZNiF@PB. However, with increasing adsorbate concentration, the vacant adsorption sites are reduced, causing the removal rate of Cd ions to decrease (Kang et al., 2022). The optimal concentration was found to be 100 mg/L for the three adsorbents and the result followed the order ZNiF@PB > ZNiF > PB. This order brings us to the conclusion that each adsorbent effectively eliminated Cd (II), but the enhanced properties of the new proposed nanocomposite materials promise better uptake and can be investigated for other heavy metal pollutants.

3.2.4. Contact time

The interaction time between ZNiF, PB, and ZNiF@PB and Cd (II) ions can impact the study outcome. Therefore, it was examined at different contact times (20–120 min). Experimental conditions such as pH, dosage (ZNiF, PB, and ZNiF@PB), temperature, and adsorbate concentration remained constant (pH: 6.0, m: 0.5g/50 ml, T: 25 °C and Co: 100 mg/L). Fig. 14 presents the removal efficiency of Cd (II) when it is in contact with the ZNiF, PB, and ZNiF@PB adsorbents. The three stages were observed, whereby the initial stage for the removal of Cd (II) by the three adsorbents occurred in the first minutes between 20 and 40 min. The uptake at this stage was very rapid. The second stage from 40 to 80 min showed a gradual increase in percentage removal, and the final stage from 80 to 120 min was observed as the equilibrium phase. A better explanation of the rapid uptake of the adsorbate by the three adsorbents at the initial time could be the result that the adsorbents have many available active sites of adsorption, making it easier for the Cd (II) ion to attach to their surface (Masuku et al., 2024; Narayana et al., 2022). Furthermore, the high concentration gradient among Cd (II) molecules and adsorbents also affect the rate (Masuku et al., 2021; Pholosi et al., 2020). However, when the contact time continued to increase from 80 to 120 min, the observed decrease was ascribed to the active sites of ZNiF@PB > ZNiF > PB responsible for the removal of cadmium, which became saturated, resulting in repulsion between the adsorbate and the adsorbent (Bai et al., 2023; Zaib and Kyung, 2022). Therefore, 80 min became the optimal contact time selected for the removal of Cd (II) by ZNiF, PB, and ZNiF@PB and the highest removal efficiency order was ZNiF@PB > ZNiF > PB.

3.3. Adsorption isotherms

The equilibrium adsorptions of the Cd ion (II) on the ZNiF, PB, and ZNiF@PB adsorbent were analyzed using isotherm models, namely Langmuir, Freundlich, and Dubinin-Radushkevish (Nchoe et al., 2023). The isotherms were fitted using a nonlinear curve and Fig. 15 illustrates the results of the adsorption of Cd (II) onto the ZNiF, PB, and ZNiF@PB adsorbent. For PB, the Langmuir isotherm had a correlation coefficient (R^2), KL, and qe were 0.98, 0.04 (L.mg/L), and 11.92 mg/g, respectively. Similarly, the values of Freundlich isotherm R^2, n, and KL were 0.97, 1.09, and 0.595 (L.mg/L), respectively. However, Dubinin-Radushkevish D-R) recorded an R^2, qe, β, and a mean free energy of 0.751, 5.15 (mg/g), 1.83 (mol^2/J^2) and 8.22 kJ/mol (E), respectively. For ZNiF, the Langmuir isotherm (R^2), KL, and qe were 0.99, 0.054 (L.mg/L), and 16.45 mg/g respectively, but for the Freundlich isotherm R^2, the value of n and KL was 0.98, 1.66 and 0.53 (L.mg/L) respectively. In the case of PB the R^2, qe, β, and E were observed to have a value of 0.760, 7.68 (mg/g), 5.73β (mol^2/J^2), and 9.34 kJ/mol (E). Lastly, the ZNiF@PB Langmuir isotherm (R^2), KL, and qe were 0.996, 0.013 (L.mg/L), and 25.273 mg/g, respectively. Freundlich isotherm with R^2, n, and KL values of 0.99, 3.438, and 0.63 (L.mg/L), respectively. Furthermore, the D-R isotherm R^2, qe, β, and E were achieved at 0.78, 7.95 (mg/g), 1.85 β (mol2/J2) and 16.41 kJ/mol. The adsorbent surface was found to contain sorption sites with an equal distribution of homogeneous active sites and energies. When comparing R^2 of the three isotherm models, the order was as follows Langmuir > Freundlich > D–R. Such results signify Cd (II) removal by ZNiF, PB, and ZNiF@PB as better modeled by the Langmuir isotherm, suggesting that the uptake favors monolayer adsorption. The qe sequence was ZNiF@PB > ZNiF > PB whereby the formation of the ZNiF@PB nanocomposite resulted in enhanced maximum adsorption capacities because of the additional binding sites introduced on the ZNiF surface groups from the PB adsorbent. Furthermore, the combined surface area (ZNiF and PB) further influences the nanocomposite qe. The value of the D-R isotherm model E gives insight into whether the sorption process is physical or chemical (Masuku et al., 2024). In this case, the calculated E values for

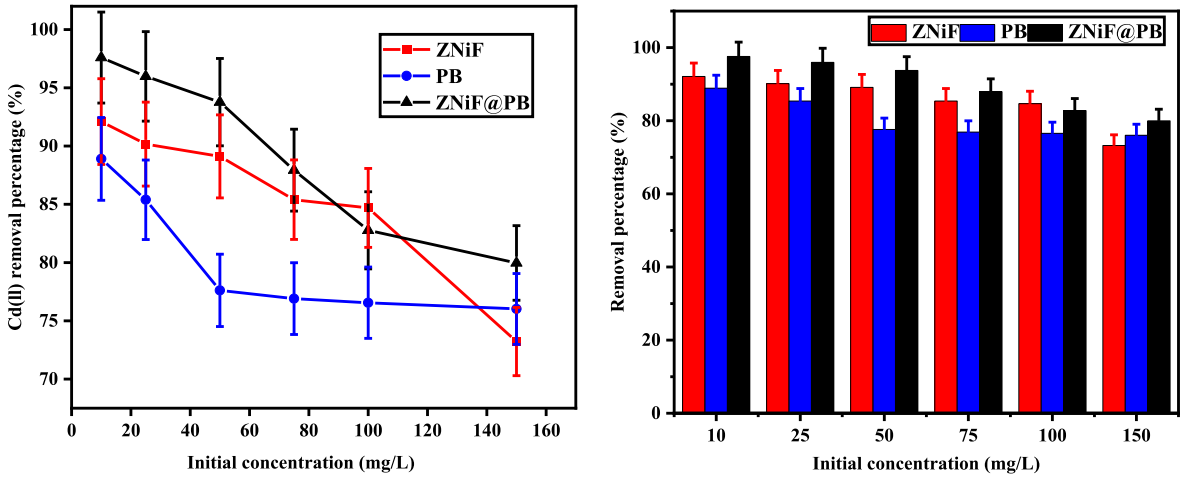

Fig. 13. Influence of initial concentration on Cd removal (II) using the prepared ZNiF, PB, and ZNiF@PB under experimental conditions of initial Cd concentration pH 6.0, adsorbent dose 0.5g/50 mL, initial concentration 10–150 mg/L, temperature: 25 °C and time 120 min.

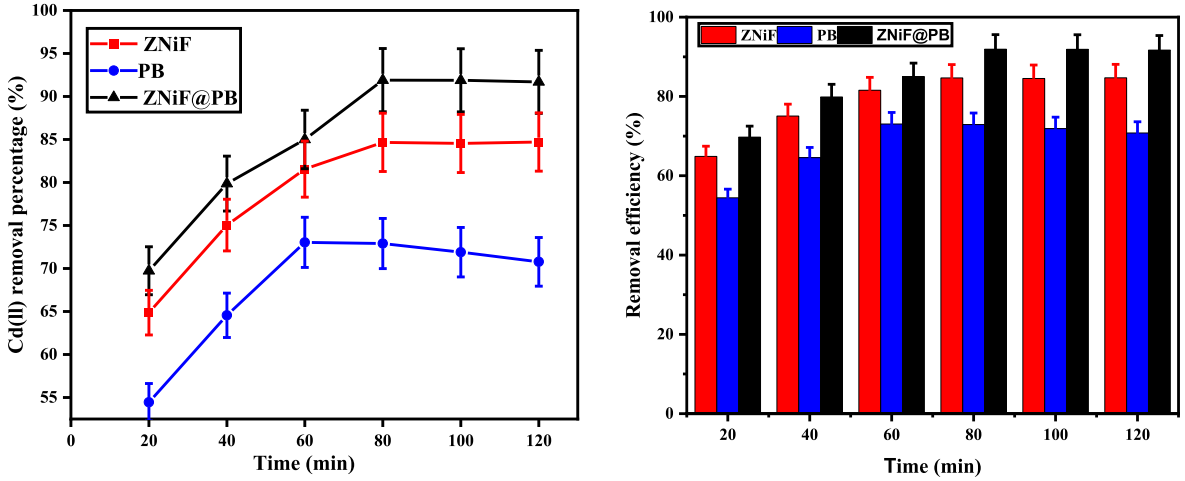

Fig. 14. The influence of contact time on the removal of Cd (II) by ZNiF, PB, and ZNiF@PB under experimental conditions: pH: 6.0, time: 20–120 min, concentration: 100 mg/L, dosage: 0.5 g/50 mL, and temperature: 25 °C.

all three adsorbents ranged from 8.22 kJ mol-1 to 16.41 kJ mol-1, suggesting that the adsorption of Cd (II) by ZNiF, PB, and ZNiF @ PB was considered chemical mode (E > 8 kJ/mol) (see Table 1).

3.4. Adsorption kinetics

The mechanism of Cd (II) adsorption by ZNiF, PB, and ZNiF@PB can be determined by modeling the experimental findings using kinetic models (Table 2 and Fig. 16). The pseudo-first-order (PFO), pseudo-second-order (PSO), and intraparticle diffusion (IPD) models have been used due to their simplicity and ease of interpretation (Kakavandi et al., 2013; Masuku et al., 2024). Fig. 16 and Table 2 illustrate the data fitted to the three kinetic models. For ZNiF nanoparticles, the correlation coefficient (R^2) values for all three kinetic models were in the order PSO ($R^2 = 0.99$) > PFO ($R^2 = 0.99$) > IPD ($R^2 = 0.72$). Similarly, for the PB nanoparticles, the R^2 values for all three kinetic models were in the order PSO ($R^2 = 0.99$) > PFO ($R^2 = 0.98$) > IPD ($R^2 = 0.87$). Similarly, for the ZNiF@PB nanocomposite, the R^2 values for the three kinetic models were in order PSO ($R^2 = 0.999$) > PFO ($R^2 = 0.998$) > IPD ($R^2 = 0.808$). Looking at the results of ZNiF, PB, and ZNiF@PB, the PSO model describes the adsorption studies since its R^2 is close to unity and the order of the most effective adsorbent followed ZNiF@PB > ZNiF > PB. In addition, the qe values were comparable to the experimental results. The PSO kinetic model proposed that the nature of adsorption is chemisorption, which occurs through electron exchange between the Cd (II) ion and the adsorptive sites ZNiF, PB, and ZNiF@PB. In the case of the IPD model, three stages were observed where the first stage is the diffusion of the boundary layer of Cd molecules (II) in solution to the outer surface of ZNiF, PB, and ZNiF@PB (Masuku et al., 2024). The second stage occurs when Cd molecules (II) diffuse into ZNiF, PB, and ZNiF@PB whereby the IPD process becomes the rate-limiting step, and the third stage known as an equilibrium stage occurs due to the internal and external rate movements of Cd molecules (II) on the ZNiF, PB, and ZNiF@PB surface (Masuku et al., 2024). Clearly, the results state that the kinetic model of IPD does not determine the rate since the plots did not pass through the line of origin (Masuku et al., 2024; Narayana et al., 2022). Therefore, it can be assumed that all of the three explored models contributed to the removal of Cd by the three adsorbents and that the uptake occurred at the same time. Therefore, the interaction was assumed π–π interaction - and the pore-filling interactions had an impact on Cd (II) removal (Masuku et al., 2024; Narayana et al., 2022).

3.5. Thermodynamic studies

The importance of this parameter in adsorption studies is to determine whether the occurring adsorption process is spontaneous or nonspontaneous (Abewaa et al., 2023). Thermodynamics further distinguishes whether the process is exothermic or endothermic, and adsorption feasibility and activation energy are also provided. For the present study, thermodynamic investigations on the removal of Cd (II) by ZNiF, PB, and ZNiF@PB were performed by varying the temperatures 25, 35, 45, and 55 °C. Other variables were maintained at optimal values (pH: 6.0, m 0.5g/50 mL, time 80 min, and concentration 100 mg/L). To determine the three important parameters, the study used the Van't Hoff equations, which are changes in enthalpy (ΔH), Gibbs free energy (ΔG), and entropy (ΔS) (Masuku et al., 2024; Narayana et al., 2022). Table 3 summarizes the results of the thermodynamic parameters for the present study. For all adsorbents, the range for ΔG was between −3.5 and 19.7 kJ/mol. Furthermore, ΔG being negative implies that the adsorption of Cd (II) on ZNiF, PB, and ZNiF@PB toward the adsorbents was spontaneous and feasible. This also indicates the affinity of ZNiF, PB, and ZNiF@PB towards the Cd (II). It should also be noted that ΔG values were more negative at higher temperatures, which can be represented as endothermic processes. The positive values of ΔH for the three adsorbents also imply that the adsorption of Cd (II) in the adsorbent of ZNiF, PB, and ZNiF@PB was endothermic. The calculated values of ΔH were below 40 kJ/mol, which favored physisorption. ΔS being (+) shows enhanced randomness at the solid-liquid adsorption interface in Cd (II) adsorption at the active sites of ZNiF, PB, and ZNiF@PB.

3.6. Reusability of adsorbents

For a potential practical application of the prepared ZNiF, PB, and ZNiF@PB, the evaluation of reusability and stability remains the subject of key importance. The effective remediation of Cd (II) by ZNiF, PB, and ZNiF@PB was studied for five consecutive cycles, and the results are illustrated in Fig. 17. There was a reduction in the activity of PB compared to those of the ZNiF and the ZNiF@PB nanocomposite. In the first cycle, when using Cd (II) 100 mg/L and ZNiF, PB, and ZNiF @ PB 0.5g/50 mL, the removal efficiency of Cd (II) was 83% for ZNiF@PB, 79% for ZNiF and 68% for PB at 120 min reaction time. However, the Cd (II) removal efficiency in the fifth cycle was recorded to be 67% for ZNiF@PB, 63% for ZNiF, and 51 % for PB. A possible reason for the higher Cd (II) removal efficiency even at the fifth cycle suggests that ZNiF and ZNiF@PB had higher reusability and stability compared to those of PB. The reusability order followed ZNiF@PB > ZNiF > PB. Previous studies on the use of nanocomposite also confirm that the modified nanoparticles had higher reusability and stability in solution than pristine materials, and these results could be due to enhanced properties of the nanocomposite, as it contains properties of the pristine

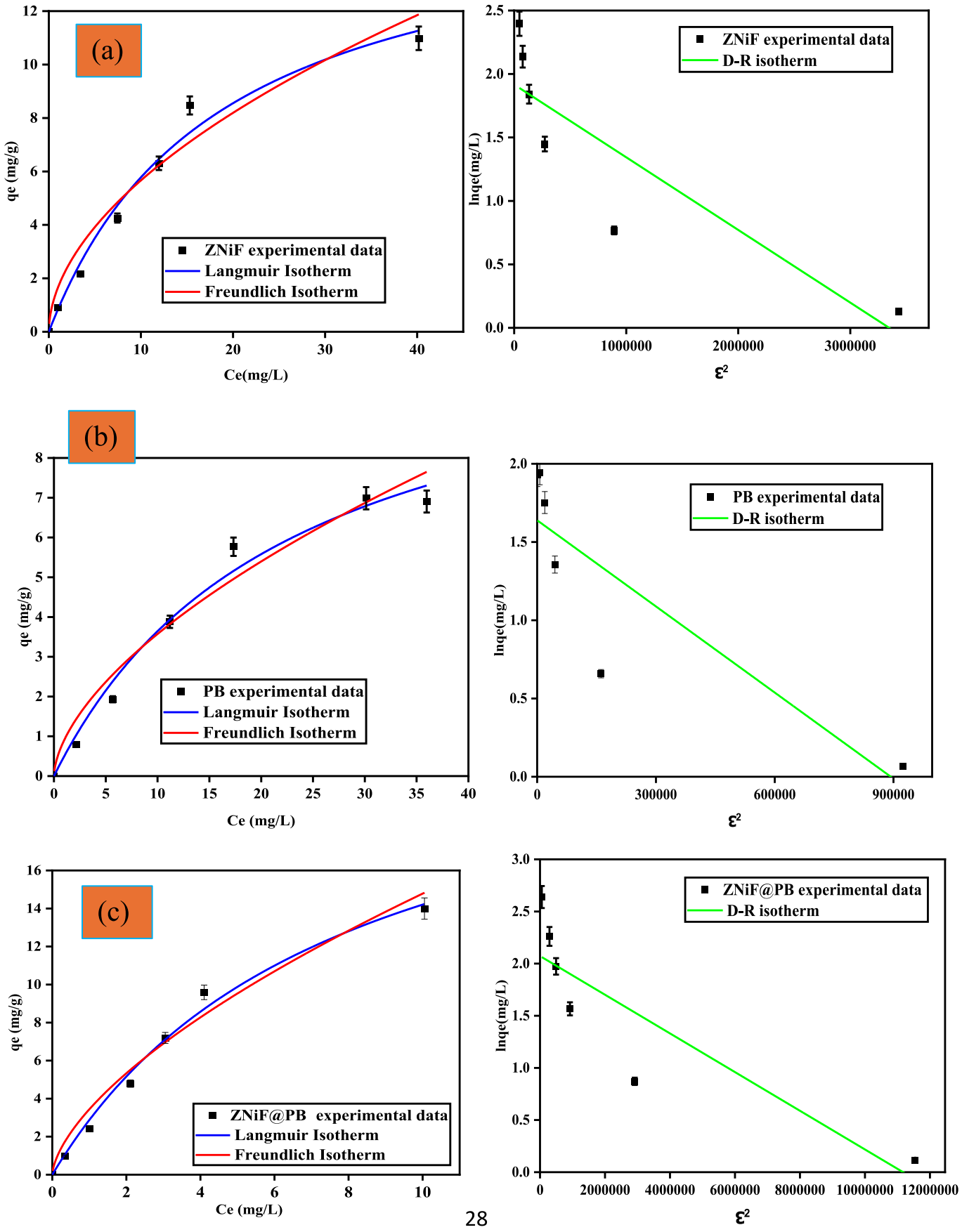

28

Fig. 15. Langmuir, Freundlich, and Dubinin-Radushkevish nonlinear fitting adsorption isotherm models under experimental conditions: dose 0.5 g/50 mL, pH: 6.0, 80 min, concentration: 100 mg/L and temperature: 25–55 °C.

Table 1
Textural properties.

Sample	BET surface area (m^2/g)	Pore volume (cm^3/g)	Pore size (nm)
ZNiF	78.4	0.34	14.9
PB	125	1.4	0.07
ZNiF@PB	104	0.12	3.14

Table 2
Kinetics studies of the uptake of Cd (II) by ZNiF, PB, and ZNiF@PB.

	Kinetic Models					
	Pseudo first order		Pseudo second order		Intraparticle	
ZNiF	Exp. qe (mg/g)	8.470	Exp. qe (mg/g)	8.470	Kdiff	0.585
	Model qe (mg/g)	9.710	Model qe (mg/g)	8.419	C	3.177
	k_1 (g/mg min)	0.072	k_1 (g/mg min)	0.016	R^2	0.723
	R^2	0.998	R^2	0.999		
PB	Exp. qe (mg/g)	6.987	Exp. qe (mg/g)	6.987	Kdiff	0.583
	Model qe (mg/g)	8.155	Model qe (mg/g)	7.183	C	1.992
	k_1 (g/mg min)	0.069	k_1 (g/mg min)	0.013	R^2	0.866
	R^2	0.979	R^2	0.995		
ZNiF@PB	Exp. qe (mg/g)	9.171	Exp. qe (mg/g)	9.171	Kdiff	0.596
	Model qe (mg/g)	9. 936	Model qe (mg/g)	9.014	C	3.603
	k_1 (g/mg min)	0.068	k_1 (g/mg min)	0.010	R^2	0.808
	R^2	0.998	R^2	0.999		

PB and pristine ZNiF nanoparticles (Masuku et al., 2024). Specifically, the improved properties of the nanocomposite that may play a good role are surface area, particle size, and magnetism. Because the PB adheres to the ZNiF surface, it can play a crucial role in increasing the adsorptive activity of the as-synthesized nanocomposite and limiting or preventing the agglomeration of the nanoparticles. Therefore, this can enhance the service life of the nanocomposite (Masuku et al., 2024; Narayana et al., 2022). The bare ZNiF nanoparticles will agglomerate, thereby reducing the dispersibility of the sample as a result of van der Waals forces and magnetism, while for the pristine PB, some of the functional groups could be affected or destroyed during application. Therefore, the study

Table 3
Thermodynamic investigations of Cd (II) uptake in the prepared ZNiF, PB, and ZNiF@PB.

Adsorbent		Thermodynamic parameters		
	T (° C)	ΔG (kJ/mol)	ΔH (kJ/mol)	ΔS (J/K mol)
ZNiF	25	−18.0		
	35	−18.5		
	45	−18.9	24.8	60.2
	55	−19.7		
PB	25	−11.0		
	35	−11.4		
	45	−11.7	17.7	37.0
	55	−12.2		
ZNiF@PB	25	−3.5		
	35	−3.7		
	45	−3.9	10.1	12.2
	55	−4.1		

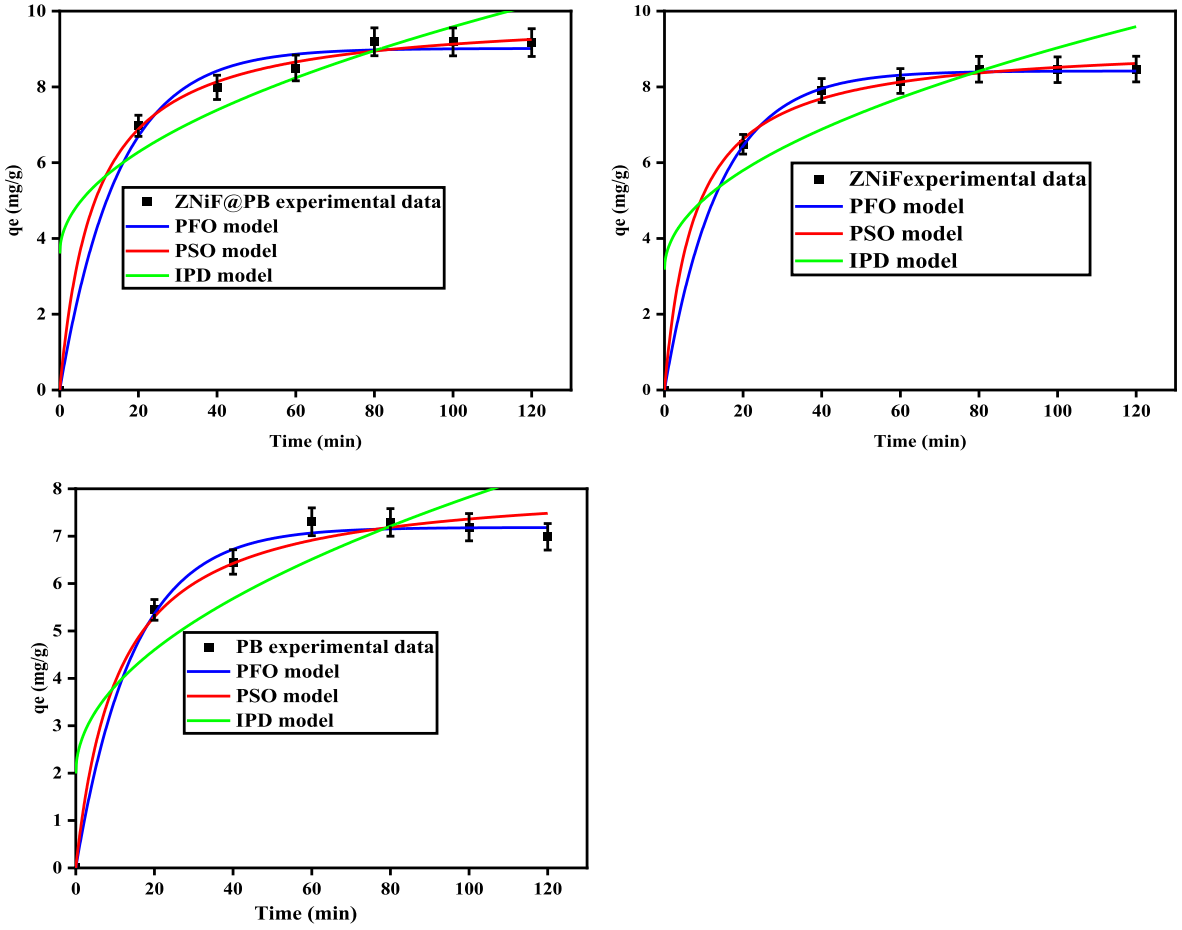

Fig. 16. Nonlinear PFO and PSO fitting of the kinetics model and the intraparticle diffusion model under experimental conditions: pH: 6.0, initial concentration: 100 mg/L, time: 20–120 min, dosage: 0.5g/50 mL and temperature: 25 °C.

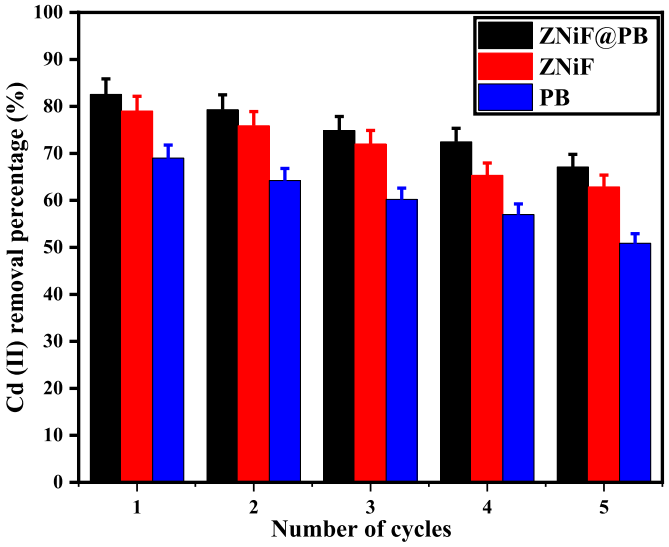

Fig. 17. Reusability studies of ZNiF, PB, and ZNiF @PB nanocomposite for the removal of Cd (II) under experimental conditions: pH: 6.0, initial Cd concentration 100 mg/L, contact time 80 min, adsorbent dosage: 0.5g/50 L and temperature 25 °C.

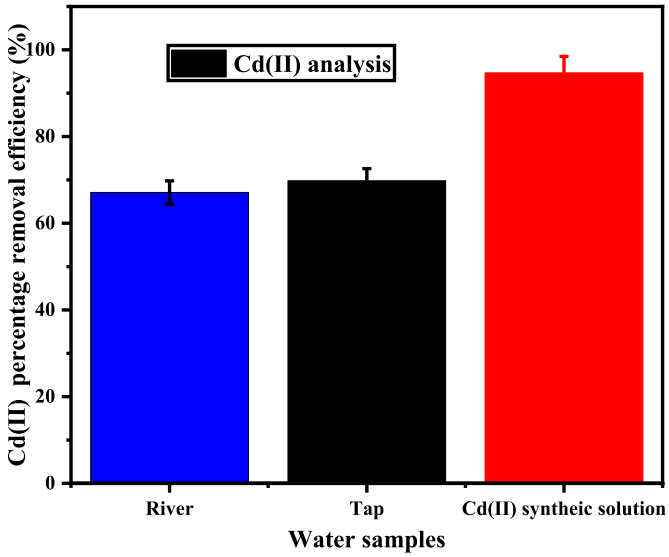

Fig. 18. Cd (II) removal using ZNiF@PB nanocomposite from a tap, river, and synthetic water solution.

suggests that the ZNiF@PB nanocomposite shows higher stability, reactivity, and reusability, which is recommended for practical engineering applications.

3.7. Adsorption of Cd (II) from real water

The preparation of nanomaterials as adsorbents for the removal of pollutants from wastewater is driven by production processes in wastewater treatment plants with less or no release of harmful contaminants into the environment after the completion of the adsorption process. Industries that use Cd (II) for manufacturing purposes and then produce a large volume of Cd effluent need to have methods that are cost-effective and efficient for handling the generated wastewater to minimize the direct discharge of Cd (II) ions into the environment. In this study, the removal of the Cd (II) target pollutant from wastewater was investigated using two types of water samples, namely tap and river water samples. River water samples were collected from a small river near the Unisa Florida campus (Johannesburg, South Africa). Before adding the ZNiF@PB adsorbent, the water was filtered using 0.45 μm PVDF syringe filters. Adsorption studies were carried out under the same conditions as synthetic wastewater pH: 6.0, temperature: 25°*C*, adsorbent dose: 0.5g/50 mL, and contact time: 80 min. Fig. 18 shows a comparison of the adsorption of Cd (II) on ZNiF@PB from tap and river water. To activate Cd (II) contamination, water samples (river and tap) were spiked to obtain the initial Cd (II) concentration of 10 mg/L. As observed in Fig. 18, the removal efficiency followed the synthetic solution > tap > river with a removal efficiency of 94.7% > 69.8%> 67.1 %, respectively. Although the removal efficiency of Cd (II) in tap and river water slightly declined after application, this could be because, in actual water samples, there are different types of particulate and possibly microorganisms. Furthermore, real water matrices also contain complex mixtures of inorganic and organic pollutants that cannot be easily removed (Yong et al., 2022). For example, tap and river water samples had some coexisting metals such as As, Be, Co, Cr, Cu, Li, Mg, Mo, Sb, Sr, V, Ca, Fe, Ni, Zn, and Mn ions, and these hindered the adsorption process. Generally, these other metals would compete with the ZNiF@PB adsorbent active sites when there is a decrease in the uptake of Cd (II) ions. Overall, the use of ZNiF@PB as an adsorbent for the removal of Cd (II) was successful for the synthetic solution and average for the actual water, since it showed the ability to remove more than 60%, which means that the adsorbent has the potential use in complex environments.

3.8. Metal leaching

The proposed adsorbent (ZNiF@PB) was made from metal ions of Ni, Zn, Fe, and pinecone biochar. During adsorption studies, these metallic ions can leach into treated water, causing secondary heavy-metal-ion pollution. Therefore, the study investigated the concentration of these metal leachings using the ICP-OES instrument after the adsorption process solution was filtered and analyzed. The results obtained from ICP-OES indicated that the maximum concentration of Fe, Ni, and Zn leached was 0.26 mg/L, 0.02 mg/L, and 0.03 mg/L, respectively. Compared to the allowable limits for Fe, Ni, and Zn, which are 0.3 mg/L,0.02 mg/L, and 5 mg/L in drinking water, the leaching of these metal ions was insignificant (Bumagina et al., 2024; Dey et al., 2021; Kinuthia et al., 2020; Ljubic et al., 2024; Zeng et al., 2024). Therefore, the conclusion drawn could be that during the adsorption studies, the dissolved metal concentrations of the adsorbent did not result in some noticeable toxicity, and the levels were acceptable for aquatic plants/animals and human consumption. Furthermore, during adsorption, the leaching profiles of the metals depend mainly on the type of adsorbent. The current study used the ZNiF@PB nanocomposite which is continuous with elements that are less toxic to the environment, and these spinel ferrite nanoparticles were decorated with an eco-friendly green material pinecone biochar (Fito et al., 2023b; Ma et al., 2020; Nimisha et al., 2022). The combination of two adsorbents (ZNiF and PB) with less toxicity to the environment was the main driving force for this work, and studies show that it was achieved. The ZNiF@PB was suitable for adsorption studies of Cd (II) with good and stable performance.

3.8.1. Environmental concerns, commercial capabilities, and future discussions

Novel nanocomposites of ZNiF@PB are composed of nickel, zinc, iron, and pinecone biochar. The materials, if properly handled, pose environmental challenges. Even after the adsorption studies were completed, the leachability studies showed that the concentration of these metals was very low and within the allowable limits in water. The ZNiF@PB has been proven to be capable of the removal of the carcinogen and mutagenic Cd (II) metal. Based on the porous nature of the adsorbent and its large surface area-to-volume ratio, they could be better candidates for other heavy metals such as arsenic and lead adsorption.

Furthermore, material properties could be investigated in the adsorption of organic pollutants and dyes. The synthesized ZNiF@PB could also be used for other applications in addition to wastewater treatment. It could have potential for several applications, including sensors, electronics, energy storage devices, and healthcare. Therefore, researchers in many fields can further investigate the development of this material to reveal more potential applications and commercialization of the material.

3.9. Comparison of Cd (II) removal

The study compared the removal efficiencies of the novel ZNiF@PB nanocomposite with other spinel ferrite@biochar in terms of different heavy metal removal. As shown in Table 4, the nanocomposite was shown to have a higher removal efficiency than other studies conducted. This could be ascribed to the fact that ZNiF@PB contains excellent combined properties from the ZNiF and PB. Therefore, it can be concluded that ZNiF@PB promises to be a good adsorbent and can be investigated for other heavy metals, including arsenic and lead. In addition, the added environmental advantages provided by agricultural biomass to produce biochar. The low cost of synthesizing ZNiF nanoparticles is also worth noting. For the present research studies, the entire research cost of ZNiF@PB synthesis was considered to be cost-effective. The ZNiF chemicals amounted to 34,795 ZAR/kg, which was much lower than the $MgFe_2O_4$, $CoFe_2O_4$, and $CuFe_2O_4$ reported at 45,755, 66,575, and 53,075 ZAR/kg, respectively (Masuku et al., 2024). Another calculated cost was that of the PB material, for the collection and grinding of pinecones, which amounted to 1400 ZAR/kg (Masuku et al., 2024). The costs of ZNiF @ PB nanocomposite were those of utilities (water use and electricity) estimated to be 1200 ZAR/200 L (Masuku et al., 2024). In terms of available adsorbents, spinel ferrite/CNTs or spinel ferrite/graphene oxide are potential nanocomposites. However, these coating agents are expensive compared to biochar. In addition, they have been associated with the generation of secondary toxics, which has remained the main challenge in the application of adsorption technology in water remediation. Therefore, the use of ZNiF@PB is a worthy replacement for expensive absorbents and environmentally friendly material.

3.10. Possible adsorption mechanism

4. The adsorption mechanism of heavy metals in different adsorbent materials occurs via hydrophobic interaction, electrostatic interaction, ion exchange, weak van der Waals interaction or π-π interaction, and hydrogen bonding (Akpomie et al., 2023). Usually, the adsorption process can occur through one of several interactions. The mechanism can be influenced by many factors, such as the pH of the solution, the texture of the adsorbent, and the chemical structure of the pollutants of interest. It is difficult to pinpoint exactly the interactions that work during the adsorption process. Fourier transform infrared spectroscopy has become a useful approach for studying the interactions of the adsorbate and adsorbent. The adsorption process can be predicted based on FTIR because the surface functional groups of the adsorbents influence the adsorption mechanism. The hydroxyl and aromatic carboxylic (COOH) groups mostly interact with the metals. Therefore, we expect that the removal mechanisms of Cd (II) by ZNiF@PB will involve a hydrogen bonding interaction. The intermolecular hydrogen bonds improved the surface interactions between adsorbate and adsorbent, which is envisioned to contribute to the Cd(ll) adsorption affinity of the ZNiF@PB. Similar to the case, Cd (II) adsorption onto ZNiF@PB results from a complex molecular interaction involving electrostatic interactions and the van der Waals force. The attraction between Cd (II) ions and the ZNiF@PB surface nanocomposite is greatly influenced by electrostatic forces. The Cd (II) io in aqueous solutions has a positive charge; however, the ZNiF@PB surface may have negatively charged regions that are connected to the point of zero-charge results. This enables the initial uptake of Cd (II) ions onto the ZNiF@PB surface by opening the environments for an electrostatic interaction among the positively and negatively charged species. In addition, as the Cd (II) ions become closer to the ZNiF@PB surface, the van der Waals force turns to operate. van der Waals involved dipole-dipole interactions, induced dipole interactions, and dispersion forces, which aid in the stabilization of the adsorbed species of Cd (II) on the adsorbent surface. In particular, the short-term variation in the distribution of the electrons inside the adsorbent results in induced dipole interactions. Therefore, this results in temporary dipoles that draw Cd (II) ions (Rafie et al., 2024). Furthermore, the Cd (II) ions get distributed toward the adsorbent active adsorption sites as the adsorption process advances because of the concentration gradient of Cd (II) ions among the bulk solution and the surface of the adsorbent. The Cd (II) ions go through the liquid film surrounding the adsorbent through a process known as external diffusion and migrate into the pores of the adsorbent through an internal diffusion process (Obayomi et al., 2023; Lim et al., 2024). The kinetic studies predicted the adsorbent-adsorbate interaction and the kinetic model data followed the PSO kinetic model, signifying that Cd (II) adsorption emphasizes the importance of chemisorption as the rate-controlling step during the application studies. In chemisorption, there will be exchange, transfer, or exchange of electrons among the adsorbents and the adsorbate. This justifies that the interaction between the surface of ZNiF@PB and the Cd (II) ions is mostly governed by chemical interactions and implies that the rate of adsorption is primarily dependent on the number of existing adsorption sites, as opposed to the concentration of Cd (II) ions in the solution. The Dubinin-Radushkevich isotherm reported the free energy of sorption (E), which ranged from 8 to 16 kJ/mol, suggesting a chemisorption process. In addition, the adsorption energy from the thermodynamic studies showed that the process was endothermic. Similarly, the release of heat during the

Table 4
Comparison of heavy metal removal using spinel-ferrite-coated biochar.

Adsorbents	Heavy Metals	Optimum condition dosage (g), temperature (° C), pH, concentration (mg/L), time (min)	Adsorption (capacity (mg/g)	% removal	References
$MnFe_2O_4$/Zn-Fe/Rice straw	Cd^{2+}	0.5g, 25 °C, ph = 6,100 mg/L , 30 min	15.72	75.08	Bai et al. (2023)
$MnFe_2O_4$-Zn-Fe/soybean straw	Cd^{2+}	0.5g, 25 °C, ph = 6100 mg/L25 °C, ph = 6100 mg/L , 30 min	25.73	76.87	Bai et al. (2023)
Mn Fe_2O_4–Zn ferrite/pine sawdust	Pb^{2+}	0.05g, 25 °C, pH = 5, 50 mg/L, 240 min.	95.0	80.1	Niu et al. (2020)
Mn Fe_2O_4/pinnatifida roots	Cd^{2+}	0.5g, 45 °C, pH = 6, 700 mg/L, 240 min	190.3	90.0	Jung et al. (2018)
$MnFe_2O_4$/Laminaria japonica	Sb (V)	1.0 g, 45 °C, pH = 3, 25 mg/, 360 min	14.6	90.0	Yong et al. (2022)
$CoFe_2O_4$/melon peel	Cd^{2+}	1.5g, 25 °C, pH = 5, 10 mg/L, 10 min	6.78	95.7	Ozdes and Duran (2021)
$MnFe_2O_4$/rice straw	Cd^{2+}	0.4g, 25 °C, pH = 6, 200 mg/L, 60 min	119.04	92.2	Tan et al. (2022)
Fe_3O_4/Lentinula edodes	Cr (VI)	12 g, 40 °C, pH = 3, 200 mg/L, 240 min	9.5	99.4	Wang et al. (2019)
ZNiF@PB	Cd^{2+}	0.5g, 25 °C, pH = 6, 100 mg/L, 80 min	9.5	96	This work

adsorption process further contributes to the advantageous uptake of Cd (II) in ZNiF@PB (Rafie et al., 2024). Furthermore, the spontaneity of the adsorption process, which was confirmed by the change in ΔG values was negative, highlighting that the process was viable in the ambient environment. In conclusion, the uptake of Cd (II) onto the ZNiF@PB nanocomposite could be controlled by the combination of various interactions such as hydrogen bonding, electrostatic forces, van Der Waals forces, and chemical bonding, and this conclusion is supported by the FTIR results and favored by the kinetics and thermodynamics data.

4. Conclusions

In this adsorption study, the coprecipitation method was used to synthesize ZNiF, PB, and ZNiF@PB nanocomposites. The three materials were further successfully used for Cd (II) adsorption from stimulated and real wastewater. The existence of carbonyls (C=O), aromatic hydroxyls/carboxylic (COOH), (C-O), and Fe-O functional groups on the FTIR spectrum of ZNiF@PB confirmed the interaction of the spinel ferrite and biochar. The surface area of ZNiF, PB, and ZNiF @ PB was calculated to be 78.4 m^2/g, 125 m^2/g, and 104 m^2/g, respectively. These surface areas significantly affected adsorption, as they provided more sorption sites for Cd (II) adsorption. The maximum Cd (II) removal of 96% was achieved at the experimental conditions of pH 6, dosage 0.5g/50 mL, initial Cd (II) concentration 100 mg/L, and contact time 80 min. Furthermore, the Langmuir model described Cd (II) uptake well, showing a monolayer adsorption process. The pseudo second-order model fits the experimental data and had an R^2 of 0.99 which favors the chemisorption process. Similarly, the thermodynamic investigations indicated the adsorption process was spontaneous and resembled an endothermic reaction with a high degree of randomness. The regeneration of ZNiF, PB, and ZNiF@PB was carried out in up to 5 cycles of which the 3 cycles were effective. Therefore, the attained results conclude that these adsorbent materials can effectively remediate Cd (II) from wastewater which could extend to clearing-ups of other heavy metal contaminants with the possibility of industrial application.

CRediT authorship contribution statement

Makhosazana Masuku: Writing – review & editing, Writing – original draft, Visualization, Software, Resources, Methodology, Formal analysis, Data curation, Conceptualization. **Jemal Fito Nure:** Writing – review & editing, Writing – original draft, Visualization, Validation, Supervision, Project administration, Methodology, Formal analysis, Conceptualization. **Harrison I. Atagana:** Writing – review & editing, Resources, Project administration, Funding acquisition, Conceptualization. **Ntuthuko Hlongwa:** Writing – review & editing, Supervision, Resources, Project administration, Funding acquisition, Conceptualization. **Thabo T.I. Nkambule:** Writing – review & editing, Supervision, Funding acquisition, Conceptualization.

Consent to participate

Not applicable.

Consent to publish

Not applicable.

Ethical approval

Not applicable.

Availability of data and materials

All data are fully available without restriction from the corresponding authors.

Funding

This research was funded by the University of South Africa **(UNISA).**

Declaration of competing interest

The authors declare the following financial interests/personal relationships which may be considered as potential competing interests: No one is the potential competing interest!!!

Acknowledgments

We would like to thank the University of South Africa, College of Science, Engineering, and Technology, and the Institute for Nanotechnology and Water Sustainability, Florida Science Campus, 1710, Johannesburg, South Africa, for financial support and other facilities.

Not applicable.

Data availability

Data will be made available on request.

References

Abewaa, M., Mengistu, A., Takele, T., Fito, J., Nkambule, T., 2023. Adsorptive removal of malachite green dye from aqueous solution using Rumex abyssinicus derived activated carbon. Sci. Rep. 13, 1–16. https://doi.org/10.1038/s41598-023-41957-x.

Abolfazli Behrooz, B., Oustan, S., Mirseyed Hosseini, H., Etesami, H., Padoan, E., Magnacca, G., Marsan, F.A., 2023. The importance of presoaking to improve the efficiency of MgCl2-modified and non-modified biochar in the adsorption of cadmium. Ecotoxicol. Environ. Saf. 257, 114932. https://doi.org/10.1016/j.ecoenv.2023.114932.

Adeniyi, A.G., Iwuozor, K.O., Emenike, E.C., Ogunniyi, S., Amoloye, M.A., Sagboye, P.A., 2023. One-step chemical activation for the production of engineered orange peel biochar. Emergent Mater 6, 211–221. https://doi.org/10.1007/s42247-022-00442-3.

Ahangari, A., Raygan, S., Ataie, A., 2019. Capabilities of nickel zinc ferrite and its nanocomposite with CNT for adsorption of arsenic (V) ions from wastewater. J. Environ. Chem. Eng. 7, 103493. https://doi.org/10.1016/j.jece.2019.103493.

Ahmed, W., Mehmood, S., Mahmood, M., Ali, S., Shakoor, A., Núñez-Delgado, A., Asghar, R.M.A., Zhao, H., Liu, W., Li, W., 2023. Adsorption of Pb(II) from wastewater using a red mud modified rice-straw biochar: influencing factors and reusability. Environ. Pollut. 326. https://doi.org/10.1016/j.envpol.2023.121405.

Akpomie, K.G., Conradie, J., Adegoke, K.A., Oyedotun, K.O., Ighalo, J.O., Amaku, J.F., Olisah, C., Adeola, A.O., Iwuozor, K.O., 2023. Adsorption mechanism and modeling of radionuclides and heavy metals onto ZnO nanoparticles: a review. Appl. Water Sci. 13, 1–24. https://doi.org/10.1007/s13201-022-01827-9.

Ali, S.M., El Mansop, M.A., Galal, A., Abd El Wahab, S.M., El-Etr, W.M.T., Zein El-Abdeen, H.A., 2023. A correlation of the adsorption capacity of perovskite/biochar composite with the metal ion characteristics. Sci. Rep. 13, 1–10. https://doi.org/10.1038/s41598-023-36592-5.

Alorabi, A.Q., Shamshi Hassan, M., Azizi, M., Sagheer, A., Mohsen, Z., Abdallah, M., Alzahrani, W., Ali, M., Alzahrani, K., Mohammed, O., Alghamdi, S., Faez, M., Alharthi, F., 2022. Corrigendum to "Fe3O4-CuO-activated carbon composite as an efficient adsorbent for bromophenol blue dye removal from aqueous solutions". Arab. J. Chem. 13 (11). https://doi.org/10.1016/j.arabjc.2021.103508 (2020) 8080–8091] (Arabian Journal of Chemistry (2020) 13(11) (8080–8091), (S1878535220303737),. Arab. J. Chem. 15, 8080–8091.

Amen, R., Yaseen, M., Mukhtar, A., Klemeš, J.J., Saqib, S., Ullah, S., Al-Sehemi, A.G., Rafiq, S., Babar, M., Fatt, C.L., Ibrahim, M., Asif, S., Qureshi, K.S., Akbar, M.M., Bokhari, A., 2020. Lead and cadmium removal from wastewater using eco-friendly biochar adsorbent derived from rice husk, wheat straw, and corncob. Clean. Eng. Technol. 1. https://doi.org/10.1016/j.clet.2020.100006.

Asadi, R., Abdollahi, H., Gharabaghi, M., Boroumand, Z., 2020. Effective removal of Zn (II) ions from aqueous solution by the magnetic MnFe2O4 and CoFe2O4 spinel ferrite nanoparticles with focuses on synthesis, characterization, adsorption, and desorption. Adv. Powder Technol. 31, 1480–1489. https://doi.org/10.1016/j.apt.2020.01.028.

Azari, A., Kakavandi, B., Kalantary, R.R., Ahmadi, E., Gholami, M., Torkshavand, Z., Azizi, M., 2015. Rapid and efficient magnetically removal of heavy metals by magnetite-activated carbon composite: a statistical design approach. J. Porous Mater. 22, 1083–1096. https://doi.org/10.1007/s10934-015-9983-z.

Babaei, A.A., Baboli, Z., Jaafarzadeh, N., Goudarzi, G., Bahrami, M., Ahmadi, M., 2015. Synthesis, performance, and nonlinear modeling of modified nano-sized magnetite for removal of Cr(VI) from aqueous solutions. Desalin. Water Treat. 53, 768–777. https://doi.org/10.1080/19443994.2013.846238.

Bai, M., Chai, Y., Chen, A., Yuan, J., Shang, C., Peng, L., Peng, C., 2023. Enhancing cadmium removal efficiency through spinel ferrites modified biochar derived from

agricultural waste straw. J. Environ. Chem. Eng. 11, 109027. https://doi.org/10.1016/j.jece.2022.109027.
Bashar, M.A., Molla, M.T.H., Chandra, D., Malitha, M.D., Islam, M.S., Rahman, M.S., Ahsan, M.S., 2023. Hydrothermal synthesis of cobalt substitute zinc-ferrite (Co1-xZnxFe2O4) nanodot, functionalised by polyaniline with enhanced photocatalytic activity under visible light irradiation. Heliyon 9, e15381. https://doi.org/10.1016/j.heliyon.2023.e15381.
Belaiche, Y., Minaoui, K., Ouadou, M., Mouhib, Y., Elansary, M., 2022. Elaboration and experimental investigation of Zn-Ni-Co spinel ferrite multi-doped rare-earth (Gd, Er, and Sm) prepared by coprecipitation method. J. Supercond. Nov. Magn. 35, 1269–1280. https://doi.org/10.1007/s10948-022-06189-6.
Bumagina, N.A., Ksenofontov, A.A., Antina, E.V., Berezin, M.B., 2024. The new role of dipyrromethene chemosensor for absorbance-ratiometic and fluorescence "turn-on" sensing Zn2+ ions in water-organic solutions and real water samples. Spectrochim. Acta Part A Mol. Biomol. Spectrosc. 307, 123663. https://doi.org/10.1016/j.saa.2023.123663.
Chakhtouna, H., Benzeid, H., Zari, N., Qaiss, A., Bouhfid, R., 2021. Functional $CoFe_2O_4$-modified biochar derived from banana pseudostem as an efficient adsorbent for the removal of amoxicillin from water. Sep. Purif. Technol. 266, 118592. https://doi.org/10.1016/j.seppur.2021.118592.
Chatzimichailidou, S., Xanthopoulou, M., Tolkou, A.K., Katsoyiannis, I.A., 2023. Biochar derived from rice by-products for arsenic and chromium removal by adsorption: a review. J. Compos. Sci. 7. https://doi.org/10.3390/jcs7020059.
Cheng, Y., Wang, B., Yan, P., Shen, J., Kang, J., Zhao, S., Zhu, X., Shen, L., Wang, S., Shen, Y., Chen, Z., 2023. In-situ formation of surface reactive oxygen species on defective sites over N-doped biochar in catalytic ozonation. Chem. Eng. J. 454, 140232. https://doi.org/10.1016/j.cej.2022.140232.
Chia, C.H., Gong, B., Joseph, S.D., Marjo, C.E., Munroe, P., Rich, A.M., 2012. Imaging of mineral-enriched biochar by FTIR, Raman and SEM-EDX. Vib. Spectrosc. 62, 248–257. https://doi.org/10.1016/j.vibspec.2012.06.006.
Dave, P.N., Sirach, R., 2023. Thermal decomposition study of ammonium nitrate in the presence of nickel-zinc ferrite additive. Catal. Commun. 177, 106639. https://doi.org/10.1016/j.catcom.2023.106639.
Dehghani Dastjerdi, O., Shokrollahi, H., Mirshekari, S., 2023. A review of synthesis, characterization, and magnetic properties of soft spinel ferrites. Inorg. Chem. Commun. 153, 110797. https://doi.org/10.1016/j.inoche.2023.110797.
Deng, Y., Huang, S., Laird, D.A., Wang, X., Meng, Z., 2019. Adsorption behaviour and mechanisms of cadmium and nickel on rice straw biochars in single- and binary-metal systems. Chemosphere 218, 308–318. https://doi.org/10.1016/j.chemosphere.2018.11.081.
Dey, M., Akter, A., Islam, S., Chandra Dey, S., Choudhury, T.R., Fatema, K.J., Begum, B. A., 2021. Assessment of contamination level, pollution risk and source apportionment of heavy metals in the Halda River water, Bangladesh. Heliyon 7, e08625. https://doi.org/10.1016/j.heliyon.2021.e08625.
Dhiman, P., Rana, G., Alshgari, R.A., Kumar, A., Sharma, G., Naushad, M., Alothman, Z. A., 2023. Magnetic Ni–Zn ferrite anchored on g-C3N4 as nano-photocatalyst for efficient photo-degradation of doxycycline from water. Environ. Res. 216, 114665. https://doi.org/10.1016/j.envres.2022.114665.
Dobrzyńska, J., Wysokińska, A., Olchowski, R., 2022. Raspberry stalks-derived biochar, magnetic biochar and urea modified magnetic biochar - synthesis, characterization and application for As(V) and Cr(VI) removal from river water. J. Environ. Manage. 316. https://doi.org/10.1016/j.jenvman.2022.115260.
Eshun, J., Wang, L., Ansah, E., Shahbazi, A., Schimmel, K., Kabadi, V., Aravamudhan, S., 2019. Characterization of the physicochemical and structural evolution of biomass particles during combined pyrolysis and CO2 gasification. J. Energy Inst. 92, 82–93. https://doi.org/10.1016/j.joei.2017.11.003.
Fito, J., Abewaa, M., Mengistu, A., Angassa, K., Ambaye, A.D., Moyo, W., Nkambule, T., 2023a. Adsorption of methylene blue from textile industrial wastewater using activated carbon developed from Rumex abyssinicus plant. Sci. Rep. 13, 1–17. https://doi.org/10.1038/s41598-023-32341-w.
Fito, J., Abewaa, M., Nkambule, T., 2023b. Magnetite-impregnated biochar of parthenium hysterophorus for adsorption of Cr(VI) from tannery industrial wastewater. Appl. Water Sci. 13, 1–23. https://doi.org/10.1007/s13201-023-01880-y.
Fito, J., Nkambule, T.T.I., 2023. Synthesis of biochar-CoFe2O4 nanocomposite for adsorption of methylparaben from wastewater under full factorial experimental design. Environ. Monit. Assess. 195. https://doi.org/10.1007/s10661-022-10819-w.
Fito, J., Tibebu, S., Nkambule, T.T.I., 2023c. Optimization of Cr (VI) removal from aqueous solution with activated carbon derived from Eichhornia crassipes under response surface methodology. BMC Chem 17, 1–19. https://doi.org/10.1186/s13065-023-00913-6.
Guo, S., Gao, Y., Wang, Y., Liu, Z., Wei, X., Peng, P., Xiao, B., Yang, Y., 2019. Urea/ZnCl2 in situ hydrothermal carbonization of Camellia sinensis waste to prepare N-doped biochar for heavy metal removal. Environ. Sci. Pollut. Res. 26, 30365–30373. https://doi.org/10.1007/s11356-019-06194-8.
Guo, Z., Chen, R., Yang, R., Yang, F., Chen, J., Li, Y., Zhou, R., Xu, J., 2020. Synthesis of amino-functionalized biochar/spinel ferrite magnetic composites for low-cost and efficient elimination of Ni(II) from wastewater. Sci. Total Environ. 722, 137822. https://doi.org/10.1016/j.scitotenv.2020.137822.
Hashem, M.A., Mim, M.W., Noshin, N., Maoya, M., 2024. Chromium adsorption capacity from tannery wastewater on thermally activated adsorbent derived from kitchen waste biomass. Clean. Water 1, 100001. https://doi.org/10.1016/j.clwat.2023.100001.
Hassaan, M.A., Yılmaz, M., Helal, M., El-Nemr, M.A., Ragab, S., El Nemr, A., 2023. Isotherm and kinetic investigations of sawdust-based biochar modified by ammonia to remove methylene blue from water. Sci. Rep. 13, 1–20. https://doi.org/10.1038/s41598-023-39971-0.
Hong, Y., Zhou, W., Cheng, Z., Huang, H., Wu, Z., Liao, S., Luo, G., 2020. Magnetic, electrical, and structural properties of Mg2+-doped nickel–zinc ferrite prepared by sol–gel–SHS method. J. Mater. Sci. Mater. Electron. 31, 16975–16982. https://doi.org/10.1007/s10854-020-04254-1.
Hu, Z.T., Wang, X.F., Xiang, S., Ding, Y., Zhao, D.Y., Hu, M., Pan, Z., Varjani, S., Wong, J. W.C., Zhao, J., 2022. Self-cleaning Mn[sbnd]Zn ferrite/biochar adsorbents for effective removal of tetracycline. Sci. Total Environ. 844, 157202. https://doi.org/10.1016/j.scitotenv.2022.157202.
Jung, K.W., Lee, S.Y., Lee, Y.J., 2018. Facile one-pot hydrothermal synthesis of cubic spinel-type manganese ferrite/biochar composites for environmental remediation of heavy metals from aqueous solutions. Bioresour. Technol. 261, 1–9. https://doi.org/10.1016/j.biortech.2018.04.003.
Kakavandi, B., Jafari, A.J., Kalantary, R.R., Nasseri, S., Ameri, A., Esrafily, A., 2013. Synthesis and properties of Fe3O4-activated carbon magnetic nanoparticles for removal of aniline from aqueous solution: equilibrium, kinetic and thermodynamic studies. J. Environ. Heal. Sci. Eng. 10, 2–10.
Kakavandi, B., Kalantary, R.R., Farzadkia, M., Mahvi, A.H., Esrafili, A., Azari, A., Yari, A. R., Javid, A.B., 2014. Enhanced chromium (VI) removal using activated carbon modified by zero valent iron and silver bimetallic nanoparticles. J. Environ. Heal. Sci. Eng. 12, 1–10. https://doi.org/10.1186/s40201-014-0115-5.
Kakavandi, B., Raofi, A., Peyghambarzadeh, S.M., Ramavandi, B., Niri, M.H., Ahmadi, M., 2018. Efficient adsorption of cobalt on chemical modified activated carbon: characterization, optimization and modeling studies. Desalin. Water Treat. 111, 310–321. https://doi.org/10.5004/dwt.2018.22238.
Kang, X., Geng, N., Li, Y., Li, X., Yu, J., Gao, S., Wang, H., Pan, H., Yang, Q., Zhuge, Y., Lou, Y., 2022. Treatment of cadmium and zinc-contaminated water systems using modified biochar: contaminant uptake, adsorption ability, and mechanism. Bioresour. Technol. 363. https://doi.org/10.1016/j.biortech.2022.127817.
Khan, B.A., Ahmad, M., Iqbal, S., Ullah, F., Bolan, N., Solaiman, Z.M., Shafique, M.A., Siddique, K.H.M., 2023. Adsorption and immobilization performance of pine-cone pristine and engineered biochars for antimony in aqueous solution and military shooting range soil: an integrated novel approach. Environ. Pollut. 317, 120723. https://doi.org/10.1016/j.envpol.2022.120723.
Kinuthia, G.K., Ngure, V., Beti, D., Lugalia, R., Wangila, A., Kamau, L., 2020. Levels of heavy metals in wastewater and soil samples from open drainage channels in Nairobi, Kenya: community health implication. Sci. Rep. 10, 1–13. https://doi.org/10.1038/s41598-020-65359-5.
Lee, J.E., Park, Y.K., 2020. Applications of modified biochar-based materials for the removal of environment pollutants: a mini review. Sustain. Times 12. https://doi.org/10.3390/su12156112.
Li, Y., Ma, S., Xu, S., Fu, H., Li, Z., Li, K., Sheng, K., Du, J., Lu, X., Li, X., Liu, S., 2020. Novel magnetic biochar as an activator for peroxymonosulfate to degrade bisphenol A: emphasizing the synergistic effect between graphitized structure and CoFe2O4. Chem. Eng. J. 387. https://doi.org/10.1016/j.cej.2020.124094.
Li, Z., Deng, L., Kinloch, I.A., Young, R.J., 2023. Raman spectroscopy of carbon materials and their composites: graphene, nanotubes and fibres. Prog. Mater. Sci. 135, 101089. https://doi.org/10.1016/j.pmatsci.2023.101089.
Liang, H., Zhu, C., Wang, A., Chen, F., 2024. Facile preparation of NiFe2O4/biochar composite adsorbent for efficient adsorption removal of antibiotics in water. Carbon Res 3. https://doi.org/10.1007/s44246-023-00094-w.
Limmun, Wanida, Limmun, Warunee, Borkowski, J.J., Ishikawa, N., Pairintra, R., Chungcharoen, T., Phanchindawan, N., Maneesri, W., Pewpa, O., Ito, A., 2024. Eco-friendly magnetic biochar from Leb Mu Nang banana peel: response surface methodology optimization for Cd(II) adsorption from synthetic wastewater. Bioresour. Technol. Reports 25, 101743. https://doi.org/10.1016/j.biteb.2023.101743.
Liu, X., Liao, J., Song, H., Yang, Y., Guan, C., Zhang, Z., 2019. A biochar-based route for environmentally friendly controlled release of nitrogen: urea-loaded biochar and bentonite composite. Sci. Rep. 9, 1–12. https://doi.org/10.1038/s41598-019-46065-3.
Ljubic, V., Perendija, J., Cvetkovic, S., Rogan, J., Trivunac, K., Stojanovic, M., Popovic, M., 2024. Removal of Ni2+ ions from contaminated water by new exopolysaccharide extracted from K. Oxytoca J7 as biosorbent. J. Polym. Environ. 32, 1105–1121. https://doi.org/10.1007/s10924-023-03031-5.
Llewellyn, G.C., Rihner, M.O., Hanlon, P., 2021. Jo ur na l P re of. Regul. Toxicol. Pharmacol. 105047. https://doi.org/10.1016/j.efmat.2024.02.002.
Ma, J., Wang, H., Zhang, M., Li, D., Liu, L., Yang, H., 2020. Preparation of terpyridine-functionalized paramagnetic nickel-zinc ferrite microspheres for adsorbing Pb(II), Hg(II), and Cd(II) from water. RSC Adv. 10, 39468–39477. https://doi.org/10.1039/d0ra06746f.
Mahmoud, M.E., Abouelanwar, M.E., Mahmoud, S.ElM.E., Abdel Salam, M., 2022. Adsorption behavior of silver quantum dots by a novel super magnetic CoFe2O4-biochar-polymeric nanocomposite. J. Colloid Interface Sci. 606, 1597–1608. https://doi.org/10.1016/j.jcis.2021.08.102.
Mangood, A.H., Gemeay, A.H., Abdel-Galeil, M.M., Salama, E.S., El-Shater, R.E., 2023. Evaluation of synergistic approach of spinel cadmium–copper nanoferrites as magnetic catalysts for promoting wastewater decontamination: impact of Ag ions doping. Environ. Sci. Pollut. Res. https://doi.org/10.1007/s11356-023-27170-3.
Manohar, A., Vijayakanth, V., Vinodhini, V., Chintagumpala, K., Manivasagan, P., Jang, E., Kim, K.H., 2023. Zinc- doped nickel ferrite nanoparticles for ESR, hyperhtermia and thier cytotoxicity in mouse muscle fibroblast (BLO-11) and human breast cancer (MDA-MB-231) cell lines. J. Alloys Compd. 960, 170780. https://doi.org/10.1016/j.jallcom.2023.170780.

Mapossa, A.B., Dantas, J., Silva, M.R., Kiminami, R.H.G.A., Costa, A.C.F.M., Daramola, M.O., 2020. Catalytic performance of NiFe2O4 and Ni0.3Zn0.7Fe2O4 magnetic nanoparticles during biodiesel production. Arab. J. Chem. 13, 4462–4476. https://doi.org/10.1016/j.arabjc.2019.09.003.

Massoudinejad, M., Asadi, A., Vosoughi, M., Gholami, M., kakavandi, B., Karami, M.A., 2015. A comprehensive study (kinetic, thermodynamic and equilibrium) of arsenic (V) adsorption using KMnO4 modified clinoptilolite. Korean J. Chem. Eng. 32, 2078–2086. https://doi.org/10.1007/s11814-015-0018-x.

Masuku, M., Nure, J.F., Atagana, H.I., Hlongwa, N., Nkambule, T.T.I., 2024. Advancing the development of nanocomposite adsorbent through zinc-doped nickel ferrite-pinecone biochar for removal of chromium (VI) from wastewater. Sci. Total Environ. 908, 168136. https://doi.org/10.1016/j.scitotenv.2023.168136.

Masuku, M., Nure, J.F., Atagana, H.I., Hlongwa, N., Nkambule, T.T.I., 2023a. Jo ur of. Sci. Total Environ. 168136. https://doi.org/10.1016/j.scitotenv.2023.168136.

Masuku, M., Ouma, L., Pholosi, A., 2021. Microwave assisted synthesis of oleic acid modified magnetite nanoparticles for benzene adsorption. Environ. Nanotechnology, Monit. Manag. 15, 100429. https://doi.org/10.1016/j.enmm.2021.100429.

Masuku, M., Ouma, L., Sanni, S., Pholosi, A., 2022. Optimization studies of BTX removal by magnetite coated oleic acid obtained from microwave-assisted synthesis using response surface methodology. Sci. Rep. 12, 1–13. https://doi.org/10.1038/s41598-022-22716-w.

Masuku, M., Sanni, S.O., Akpotu, S.O., Pholosi, A., 2023b. Synthesis of magnetite coated oleic acid: sequestration of toluene and xylene from aqueous solution and cost analysis. Water. Air. Soil Pollut. 234, 1–18. https://doi.org/10.1007/s11270-023-06749-z.

Mitra, S., Chakraborty, A.J., Tareq, A.M., Emran, T. Bin, Nainu, F., Khusro, A., Idris, A. M., Khandaker, M.U., Osman, H., Alhumaydhi, F.A., Simal-Gandara, J., 2022. Impact of heavy metals on the environment and human health: novel therapeutic insights to counter the toxicity. J. King Saud Univ. Sci. 34, 101865. https://doi.org/10.1016/j.jksus.2022.101865.

Mmelesi, O.K., Ammar-Merah, S., Nkambule, T.T.I., Kefeni, K.K., Kuvarega, A.T., 2023. Synergistic role of N-doped carbon quantum dots on Zn-doped cobalt ferrite (N-CQDs/ZnCF) for the enhanced photodegradation of oxytetracycline under visible light. Mater. Sci. Eng. B Solid-State Mater. Adv. Technol. 294. https://doi.org/10.1016/j.mseb.2023.116538.

Mmelesi, O.K., Patala, R., Nkambule, T.T.I., Mamba, B.B., Kefeni, K.K., Kuvarega, A.T., 2022. Effect of Zn doping on physico-chemical properties of cobalt ferrite for the photodegradation of amoxicillin and deactivation of E. coli. Colloids Surfaces A Physicochem. Eng. Asp. 649. https://doi.org/10.1016/j.colsurfa.2022.129462.

Moges, A., Nkambule, T.T.I., Fito, J., 2022. The application of GO-Fe3O4 nanocomposite for chromium adsorption from tannery industry wastewater. J. Environ. Manage. 305, 114369. https://doi.org/10.1016/j.jenvman.2021.114369.

Mokubung, K.E., Gumbi, N.N., Lau, W.J., Nxumalo, E.N., 2024. Pine cone derived polyethersulfone/biochar-Fe3O4 mixed matrix membranes for removal of arsenic from acid mine drainage. Chem. Eng. Res. Des. 201, 31–44. https://doi.org/10.1016/j.cherd.2023.11.010.

Naik, M.M., Vinuth, M., Kumar, V.U., Hemakumar, K.H., Preethi, G., Kumar, M.P., Nagaraju, G., 2023. A facile green synthesis of nickel ferrite nanoparticles using Tamarindus Indica seeds for magnetic and photocatalytic studies. Nanotechnol. Environ. Eng. 8, 143–151. https://doi.org/10.1007/s41204-022-00257-x.

Nakajima, S., Araki, S., Sasamoto, R., Kanda, Y., Yamanaka, S., 2022. Key particle properties of shells for cadmium chemisorption. Chemosphere 287, 132257. https://doi.org/10.1016/j.chemosphere.2021.132257.

Narayana, P.L., Lingamdinne, L.P., Karri, R.R., Devanesan, S., AlSalhi, M.S., Reddy, N.S., Chang, Y.Y., Koduru, J.R., 2022. Predictive capability evaluation and optimization of Pb(II) removal by reduced graphene oxide-based inverse spinel nickel ferrite nanocomposite. Environ. Res. 204, 112029. https://doi.org/10.1016/j.envres.2021.112029.

Nchoe, O.B., Sanni, S.O., Viljoen, E.L., Pholosi, A., Pakade, V.E., 2023. Surfactant-modified Macadamia nutshell for enhancement of methylene blue dye adsorption from aqueous media. Case Stud. Chem. Environ. Eng. 8, 100357. https://doi.org/10.1016/j.cscee.2023.100357.

Nimisha, O.K., Akshay, M., Mannya, S., Reena Mary, A.P., 2022. Synthesis and photocatalytic activity of nickel doped zinc ferrite. Mater. Today Proc. 66, 2370–2373. https://doi.org/10.1016/j.matpr.2022.06.332.

Niu, Z., Feng, W., Huang, H., Wang, B., Chen, L., Miao, Y., Su, S., 2020. Green synthesis of a novel Mn–Zn ferrite/biochar composite from waste batteries and pine sawdust for Pb2+ removal. Chemosphere 252, 126529. https://doi.org/10.1016/j.chemosphere.2020.126529.

Olfatmehr, N., Kakavandi, B., Khezri, S.M., 2022. Peroxydisulfate activation by enhanced catalytic activity of CoFe2O4 anchored on activated carbon: a new sulfate radical-based oxidation study on the Cefixime degradation. Sep. Purif. Technol. 302, 121991. https://doi.org/10.1016/j.seppur.2022.121991.

Omidinasab, M., Rahbar, N., Ahmadi, M., Kakavandi, B., Ghanbari, F., Kyzas, G.Z., Martinez, S.S., Jaafarzadeh, N., 2018. Removal of vanadium and palladium ions by adsorption onto magnetic chitosan nanoparticles. Environ. Sci. Pollut. Res. 25, 34262–34276. https://doi.org/10.1007/s11356-018-3137-1.

Ozdes, D., Duran, C., 2021. Preparation of melon peel biochar/CoFe2O4 as a new adsorbent for the separation and preconcentration of Cu(II), Cd(II), and Pb(II) ions by solid-phase extraction in water and vegetable samples. Environ. Monit. Assess. 193. https://doi.org/10.1007/s10661-021-09389-0.

Palacio Gómez, C.A., Barrero Meneses, C.A., Jaén, J.A., 2020. Raman, infrared and Mössbauer spectroscopic studies of solid-state synthesized Ni-Zn ferrites. J. Magn. Magn Mater. 505, 166710. https://doi.org/10.1016/j.jmmm.2020.166710.

Patel, S., Hedayati Marzbali, M., Hakeem, I.G., Veluswamy, G., Rathnayake, N., Nahar, K., Agnihotri, S., Bergmann, D., Surapaneni, A., Gupta, R., Sharma, A., Shah, K., 2023. Production of H2 and CNM from biogas decomposition using biosolids-derived biochar and the application of the CNM-coated biochar for PFAS adsorption. Waste Manag. 159, 146–153. https://doi.org/10.1016/j.wasman.2023.01.037.

Peng, H., Li, Y., Wen, J., Zheng, X., 2021. Synthesis of ZnFe2O4/B,N-codoped biochar via microwave-assisted pyrolysis for enhancing adsorption-photocatalytic elimination of tetracycline hydrochloride. Ind. Crops Prod. 172, 114066. https://doi.org/10.1016/j.indcrop.2021.114066.

Pholosi, A., Naidoo, E.B., Ofomaja, A.E., 2020. Intraparticle diffusion of Cr(VI) through biomass and magnetite coated biomass: a comparative kinetic and diffusion study. South African J. Chem. Eng. 32, 39–55. https://doi.org/10.1016/j.sajce.2020.01.005.

Punia, P., Aggarwal, R.K., Kumar, R., Dhar, R., Thakur, P., Thakur, A., 2022. Adsorption of Cd and Cr ions from industrial wastewater using Ca doped Ni–Zn nanoferrites: synthesis, characterization and isotherm analysis. Ceram. Int. 48, 18048–18056. https://doi.org/10.1016/j.ceramint.2022.02.234.

Qi, J., Zhu, H., Yang, T., Wang, X., Wang, Z., Lei, X., Li, B., Qian, W., 2024. Biomass-derived carbon/iron composite (FexOy-BC (RM)) with excellent Cd(II) adsorption from wastewater – red mud resource utilization. Arab. J. Chem. 17, 105411. https://doi.org/10.1016/j.arabjc.2023.105411.

Rafie, S.F., Abu-Zahra, N., Sabetvand, R., 2024. Enhancing Zn (II) recovery efficiency: Bi-divalent nickel–cobalt ferrite spinel NiXCo1-xFe2O4 as a Game-changing Adsorbent—an experimental and computational study. Chemosphere 362, 142702. https://doi.org/10.1016/j.chemosphere.2024.142702.

Sadezky, A., Muckenhuber, H., Grothe, H., Niessner, R., Pöschl, U., 2005. Raman microspectroscopy of soot and related carbonaceous materials: spectral analysis and structural information. Carbon N. Y. 43, 1731–1742. https://doi.org/10.1016/j.carbon.2005.02.018.

Sahoo, S.S., Vijay, V.K., Chandra, R., Kumar, H., 2021. Production and characterization of biochar produced from slow pyrolysis of pigeon pea stalk and bamboo. Clean. Eng. Technol. 3, 100101. https://doi.org/10.1016/j.clet.2021.100101.

Shakya, A., Vithanage, M., Agarwal, T., 2022. Influence of pyrolysis temperature on biochar properties and Cr(VI) adsorption from water with groundnut shell biochars: mechanistic approach. Environ. Res. 215, 114243. https://doi.org/10.1016/j.envres.2022.114243.

Sharma, A., Kumar, A.A., Mohanty, B., Khanam, S., 2023. Synthesis, characterization and thermo-kinetic analysis of sawdust biochar for adsorbent and combustion drives. Bioresour. Technol. Reports 22, 101485. https://doi.org/10.1016/j.biteb.2023.101485.

Shoukat, S., Haq, S., Rehman, W., Waseem, M., Hafeez, M., Din, S.U., Zain-ul-Abdin, Ahmad, P., Rehman, M.U., Shah, A., Khan, B., 2021. Remediation of chromium (VI) and rhodamine 6G via mixed phase nickel-zinc nanocomposite: synthesis and characterization. J. Inorg. Organomet. Polym. Mater. 31, 1565–1575. https://doi.org/10.1007/s10904-020-01776-3.

Singh, M., Rayaz, M., Arti, R., 2023. Isotherm and kinetic studies for sorption of Cr(VI) onto Prosopis cineraria leaf powder: a comparison of linear and non-linear regression analysis. Environ. Prog. Sustain. Energy. https://doi.org/10.1002/ep.14259.

Singh, N.B., Nagpal, G., Agrawal, S., Rachna, 2018. Water purification by using adsorbents: a review. Environ. Technol. Innov. 11, 187–240. https://doi.org/10.1016/j.eti.2018.05.006.

Song, J., Wang, Y., Lv, Z., Li, Y., Cao, X.Q., Cheng, W., 2023. Degradation of nonylphenol ethoxylate 10 in biochar-CoFe2O4/peroxymonosulfate system: transformation products identification, catalysis mechanism and influencing factors. J. Environ. Chem. Eng. 11, 109241. https://doi.org/10.1016/j.jece.2022.109241.

Tan, W.T., Zhou, H., Tang, S.F., Zeng, P., Gu, J.F., Liao, B.H., 2022. Enhancing Cd(II) adsorption on rice straw biochar by modification of iron and manganese oxides. Environ. Pollut. 300. https://doi.org/10.1016/j.envpol.2022.118899.

Tatarchuk, T., Myslin, M., Lapchuk, I., Shyichuk, A., Murthy, A.P., Gargula, R., Kurzydło, P., Bogacz, B.F., Pędziwiatr, A.T., 2021. Magnesium-zinc ferrites as magnetic adsorbents for Cr(VI) and Ni(II) ions removal: cation distribution and antistructure modeling. Chemosphere 270. https://doi.org/10.1016/j.chemosphere.2020.129414.

Van Vinh, N., Zafar, M., Behera, S.K., Park, H.S., 2015. Arsenic(III) removal from aqueous solution by raw and zinc-loaded pine cone biochar: equilibrium, kinetics, and thermodynamics studies. Int. J. Environ. Sci. Technol. 12, 1283–1294. https://doi.org/10.1007/s13762-014-0507-1.

Wang, C., Tan, H., Liu, H., Wu, B., Xu, F., Xu, H., 2019. A nanoscale ferroferric oxide coated biochar derived from mushroom waste to rapidly remove Cr(VI) and mechanism study. Bioresour. Technol. Reports 7, 100253. https://doi.org/10.1016/j.biteb.2019.100253.

Wang, J., Sun, M., Wang, L., Xiong, X., Yuan, W., Liu, Y., Liu, S., Zhang, Q., Liu, J., Wang, Y., Tsang, D.C.W., 2023. High-efficiency removal of arsenic(III) from wastewater using combined copper ferrite@biochar and persulfate. Chemosphere 336, 139089. https://doi.org/10.1016/j.chemosphere.2023.139089.

Wang, W.D., Cui, Y.X., Zhang, L.K., Li, Y.M., Sun, P., Han, J.H., 2021. Synthesis of a novel ZnFe2O4/porous biochar magnetic composite for Th(IV) adsorption in aqueous solutions. Int. J. Environ. Sci. Technol. 18, 2733–2746. https://doi.org/10.1007/s13762-020-03023-1.

Wani, T.A., Suresh, G., Masrour, R., Batoo, K.M., Rasool, A., 2023. A structural, morphological, optical and magnetic study of nickel-substituted zinc (Ni–Zn) ferrite nanoparticles synthesized via glycine assisted gel autocombustion synthesis route. Mater. Chem. Phys. 307, 128169. https://doi.org/10.1016/j.matchemphys.2023.128169.

Wu, Q., Xian, Y., He, Z., Zhang, Q., Wu, J., Yang, G., Zhang, X., Qi, H., Ma, J., Xiao, Y., Long, L., 2019. Adsorption characteristics of Pb(II) using biochar derived from spent

mushroom substrate. Sci. Rep. 9, 1–11. https://doi.org/10.1038/s41598-019-52554-2.

Xia, S., Tao, J., Zhao, Y., Men, Y., Chen, C., Hu, Y., Zhu, G., Chu, Y., Yan, B., Chen, G., 2024. Application of waste derived magnetic acid-base bifunctional CoFe/biochar/CaO as an efficient catalyst for biodiesel production from waste cooking oil. Chemosphere 350, 141104. https://doi.org/10.1016/j.chemosphere.2023.141104.

Yong Lee, S., Kim, H., Jang, H., Hwang, M.J., Bong Lee, K., Choi, J.W., Jung, K.W., 2022. Fabrication of manganese ferrite (MnFe2O4) microsphere-coated magnetic biochar composite for antimonate sequestration: characterization, adsorption behavior, and mechanistic understanding. Appl. Surf. Sci. 578, 152005. https://doi.org/10.1016/j.apsusc.2021.152005.

Yong, S., Kim, H., Jang, H., Hwang, M., Choi, W., Jung, K., 2022. Applied Surface Science Fabrication of manganese ferrite (MnFe 2 O 4) microsphere-coated magnetic biochar composite for antimonate sequestration : characterization , adsorption behavior , and mechanistic understanding. Appl. Surf. Sci. 578, 152005. https://doi.org/10.1016/j.apsusc.2021.152005.

Yuan, J., Wang, C., Tang, Z., Chu, T., Zheng, C., Han, Q., Chen, H., Tan, Y., 2024. Biochar derived from traditional Chinese medicine residues: an efficient adsorbent for heavy metal Pb(II). Arab. J. Chem. 17, 105606. https://doi.org/10.1016/j.arabjc.2024.105606.

Zaib, Q., Kyung, D., 2022. Optimized removal of hexavalent chromium from water using spent tea leaves treated with ascorbic acid. Sci. Rep. 12, 1–14. https://doi.org/10.1038/s41598-022-12787-0.

Zeng, H., Yang, X., Yang, Y., Liu, L., Guo, H., Xie, L., Chai, X., Xu, K., Du, G., Zhang, L., 2024. Fluorescent probes based on cellulose for sensitive detection of Fe3+ and its applications. Ind. Crops Prod. 210, 118178. https://doi.org/10.1016/j.indcrop.2024.118178.

Zeng, T., Rene, E.R., Zhang, S., Lens, P.N.L., 2019. Removal of selenate and cadmium by anaerobic granular sludge: EPS characterization and microbial community analysis. Process Saf. Environ. Prot. 126, 150–159. https://doi.org/10.1016/j.psep.2019.03.039.